In vivo properties of Arabidopsis FCA condensates involved in RNA 3' processing

Geng-Jen Jang[1], Alex L. Payne-Dwyer[2], Robert Maple[1], Zhe Wu[1,3], Fuquan Liu[1,4], Sergio G. Lopez[1], Yanning Wang[5], Xiaofeng Fang[5], Mark C. Leake[2,6] and Caroline Dean[1,*]

[1]Department of Cell and Developmental Biology, John Innes Centre, Norwich, UK

[2]School of Physics, Engineering and Technology, University of York, York, UK

[3]Institute of Plant and Food Science, Southern University of Science and Technology, Shenzhen, China

[4]Institute of Global Food Security, Queen's University Belfast, Belfast, UK

[5]Center for Plant Biology, Tsinghua University, Beijing, China.

[6]Department of Biology, University of York, York, UK

*Corresponding author, Tel: +44 (0)1603 450000; E-mail: caroline.dean@jic.ac.uk

Abstract

Our understanding of the functional requirements underpinning biomolecular condensation *in vivo* is still relatively poor. The Arabidopsis RNA binding protein FCA is found in liquid-like nuclear condensates that function in transcription termination, promoting proximal polyadenylation at many targets in the Arabidopsis genome. To further understand the properties of these condensates *in vivo* we used single particle tracking experiments on FCA reporters stably expressed at endogenous levels in plant nuclei. These revealed FCA forms a core oligomer of ~4 molecules that multimerizes into higher-order particles. This assembles into macromolecular condensates through the function of the coiled-coil protein FLL2, which is genetically required for FCA function. FLL2 predominately co-localizes with FCA in larger sized condensates. A missense mutation in the FCA RRM domain, also genetically required for FCA function, reduced both average FCA particle and condensate size but did not perturb the core oligomer. Our work points to a modular structure for FCA condensates involving multimerization of core oligomers that assemble into functional macromolecular condensates via associated RNA and FLL2 interactions.

Keywords: Biomolecular condensate/*COOLAIR*/*FLC*/Non-coding RNA/RNA processing

Introduction

Cellular compartmentalization by biomolecular condensates is associated with diverse processes in eukaryotic cells (Banani et al, 2017; Shin & Brangwynne, 2017). While *in vitro* studies have highlighted their roles in increasing local concentration and residence time of interacting components, the functional characteristics of heterogeneous condensates *in vivo* remain unclear. Plants are an excellent system in which to study biomolecular condensates due to their response to external conditions (Field et al, 2023).

For example, Arabidopsis *FLOWERING LOCUS C* (*FLC*), a gene encoding a key flowering repressor, is regulated by co-transcriptional and antisense-mediated chromatin silencing mechanisms (Fang et al, 2020; Xu et al, 2021) that involve multiple nuclear biomolecular condensates with very different properties (Berry et al, 2017; Fang et al, 2019; Zhu et al, 2021; Fiedler et al, 2022). One of those involves the RNA-binding protein FCA, which forms liquid-like nuclear condensates (Fang et al, 2019). Another involves FRIGIDA, a strong activator of *FLC* expression, which forms condensates at low temperature, with turnover dynamics that are slow compared to FCA (Zhu et al, 2021). FCA directly interacts with FY, a Pfs2p/WDR33 homologue and a central component of the polyadenylation machinery in eukaryotes (Simpson et al, 2003). FCA contains two RRM (RNA Recognition Motif) domains and a WW domain located between two predicted prion-like domains (Macknight et al, 1997). FCA recruits RNA 3' processing factors to an R-loop, which is a DNA:RNA hybrid generated by the antisense non-coding RNA, *COOLAIR*, to induce transcription-coupled chromatin repression (Xu et al, 2021; Mateo-Bonmati et al, 2024; Menon et al, 2024). This mechanism also involves an FCA-interacting coiled-coil protein, FLL2, which is required for both formation of FCA nuclear condensates and FCA function (Fang et al, 2019). *In vitro* assays revealed that FCA condensates were enhanced by addition of low amounts of Arabidopsis RNA. However, the immunoprecipitation of *COOLAIR* nascent transcripts by FCA was not dependent on FLL2 (Fang et al, 2019).

Knowledge of the properties and molecular structure of biomolecular condensates helps dissection of the molecular mechanisms involved (Peran & Mittag, 2020). However, studies of biological condensates have focused on *in vitro* analysis and transfection studies and if *in vivo* stable expression fusions have been made, they are often not carefully matched to endogenous expression levels. This will influence the *in vivo* biophysical properties (Bienz, 2020). Here, we therefore generated stable transgenic plants with fusions expressed under their own regulatory regions and chose lines that expressed the fusion at endogenous levels. Determining the biophysical properties of condensates *in vivo* in plant systems is challenging so we exploited SlimVar microscopy, a single-molecule imaging technique (Plank et al, 2009; Payne-Dwyer et al, 2024). This enables simultaneous tracking of individual particles within a wide range of biological condensates providing quantitative measurements of molecule number and molecular motion behaviour (Shen et al, 2023). This method has been used to study biomolecular condensates in live cells including bacteria, yeast or mammalian cells (Kent et al, 2020; Izeddin et al, 2014; Ladouceur et al, 2020; Biswas et al, 2022) and we adapted it for living plant tissues to specifically study nuclear proteins (Bayle et al, 2021).

Our findings indicate that FCA-mScarlet-I particles multimerize and then assemble in an FLL2-dependent manner into the liquid-like condensates observed using confocal microscopy. FLL2 and FCA predominantly co-localize in the larger condensates. The involvement of RNA in promoting FCA condensation was shown through the identification of a missense mutation in the FCA second RRM

domain. This mutation reduced RNA-binding activity *in vitro*, significantly attenuated FCA particle size and condensate formation, lowered RNA 3' processing efficiency and prevented *FLC* repression but did not influence formation of the core FCA particle. Our work points to a modular structure for RNA 3' processing FCA condensates, with a low-order oligomer core that multimerizes into higher order particles via associated RNA and into larger functionally important condensates through FLL2 interaction.

Results

Single particle tracking reveals physical characteristics of FCA particles.

For the SlimVar microscopy we chose to generate an FCA-mScarlet-I translational fusion as a fluorescent reporter. mScarlet-I is a bright red fluorescent protein known for its characteristics as a rapidly maturing monomer (Bindels et al, 2016). A mScarlet-I coding sequence was inserted into an FCA genomic clone and transgenic plant lines were generated, where the fusion was expressed at similar level as the endogenous FCA gene (Fig. EV1A and B). The FCA-mScarlet-I fusion formed nuclear foci (Fig. 1A and Fig. 3A) and rescued the *fca-9* mutant phenotype (Fig. EV1B), just like the FCA-eGFP fusion (Fang et al, 2019). We exploited SlimVar microscopy with a narrow, oblique illumination angle of 60 ± 5° to enhance imaging contrast and dynamically track very small FCA particles in nuclei in whole root tissue (Fig. 1A and Movie EV1). The single-molecule sensitivity of SlimVar *in vivo*, coupled with stepwise photobleaching of fluorescent protein tags (Leake et al, 2006; Reyes-Lamothe et al, 2010; Payne-Dwyer et al, 2024), allowed us to characterize single-molecule brightness of the FCA-mScarlet-I. This enabled quantification of the number of FCA-mScarlet-I molecules (stoichiometry) within the particles in intact tissue (Fig. EV2 and Movie EV2; Jin et al, 2021).

Single particle tracking was undertaken on homozygous transgenic plants carrying the FCA-mScarlet-I transgene expressed at endogenous levels in three biological replicate experiments. Analysis of the FCA-mScarlet-I stoichiometry distribution identified a distinct peak representing a low-order oligomer of FCA-mScarlet-I (Fig. 1B) with other peaks in multiples of approximately 4, from approximately 16 to 56 molecules (Fig. 1C). This finding aligns with a previous study that described the prion-like domain of FCA, which when fused to GFP in yeast formed small oligomers (Chakrabortee et al, 2016). To further investigate the oligomerization properties of FCA molecules we analysed in vitro produced FCA protein. Purified recombinant FCA proteins containing either the NH2-terminal half containing RRM domains (MBP-RRM, Fang et al, 2019) or the C-terminal FCA half containing prion-like domains (MBP-PrLD) -shown schematically in Fig. EV3 - were analysed using size exclusion chromatography with multi-angle static light scattering (SEC-MALS). The FCA RRM fragment forms low-order oligomers containing 4 or possibly 5 FCA proteins, consistent with the particle tracking assay *in vivo*. The prion-like C-terminal domain formed very large aggregates with more than 100 molecules (Fig.

EV3), a characteristic frequently associated with *in vitro* expression of PrLDs at relatively high concentrations.

SlimVar also enabled us to analyse the *in vivo* diffusion coefficient of individual particles with different stoichiometry. Generally, particles with low stoichiometry displayed variable mobility, while those with high stoichiometry showed low mobility (Fig. 1D). In particular, the diffusion coefficient of particles with stoichiometry less than 10 or more than 10 was 0.54 ± 0.75 $\mu m^2/s$ (mean ± s.d.) and 0.27 ± 0.4 $\mu m^2/s$, respectively.

FCA and FLL2 show co-localization in a larger size class of condensates.

Our previous study using transient assays suggested that FCA condensates serve as the sites for the interaction between FCA, FLL2 and 3'-end processing factors (Fang et al, 2019). However, the condensates formed by FCA and FLL2 exhibited different patterns in low resolution images of Arabidopsis roots (Fang et al, 2019). To investigate the potential co-localization of FCA and FLL2 within the same nuclear condensates *in vivo*, we crossed plants carrying an FCA-mTurquoise transgene (Xu et al, 2021) with plants carrying the FLL2-eYFP transgene (Fang et al, 2019) and used F3 plants expressing both reporters for imaging. 3D imaging and Airyscan confocal microscopy were used, acknowledging that the Z-axis resolution of the confocal microscope and the limitations of the imaging algorithm may underestimate the number and size of the condensates. We found that FCA-mTurquoise and FLL2-eYFP foci generally reside in distinct condensates within the cell nucleus (Fig. 2A and Appendix Fig. S1) but co-localize within a few larger condensates (Fig. 2B and D). We conducted a comprehensive analysis to determine the size distributions and the frequency of FCA, FLL2 and FCA/FLL2-co-localized condensates (Fig. 2C and Appendix Fig. S2). The *sof78* missense mutation in FLL2 is predicted to influence a salt bridge connecting two coiled coils, and this attenuates FCA condensation and R-loop resolution (Fig. EV4; Fang et al, 2019). We used single particle tracking to analyse whether *sof78* affected the assembly of the low-order oligomers of FCA. The analysis reveals that the periodicity and stoichiometry distribution of FCA particles in *sof78* shows no obvious difference compared to the control (Fig. EV4B to D). Overall, the data suggest that association of FLL2 promotes formation of the larger functional FCA condensates.

To address if these prominent FCA/FLL2 condensates directly associate with the *FLC* locus, we crossed the FCA-mScarlet-I transgene into a line carrying a previously established *FLC-lacO*/eYFP-LacI system enabling spatial localization of the *FLC* locus in the nucleus. This line also carries an active *FRIGIDA* allele so *FLC* is in an active transcriptional state (Rosa et al, 2013). FCA condensates did not frequently co-localize with the *FLC-lacO*/eYFP-LacI marked locus (Fig. EV5). This result suggests that FCA condensates may only transiently associate with the *FLC* locus in this genotype and environmental conditions. However, it will be interesting to repeat this analysis in a genotype where

148 *FLC* is transcriptionally repressed by FCA, but where the Polycomb silencing has not yet been
149 established (Menon et al, 2024).
150
151 **FCA condensation is dependent on a functional RRM domain.**
152 To further investigate the functional significance of the molecular composition in FCA condensates we
153 continued a genetic screen for factors essential for FCA function (Liu et al, 2007). We used transgenic
154 plants with overexpressed *35S::FCAγ* and conducted a forward genetic analysis to identify mutations
155 that suppressed FCA's ability to repress *FLC* expression. This identified a missense mutation on the
156 FCA overexpression transgene at amino acid 304 of the FCA protein, resulting in a leucine to
157 phenylalanine change (Fig. EV1C). This alteration is located within the second RRM domain of FCA,
158 a domain conserved across various species (Macknight et al, 1997; Fig. EV1D). That the mutant came
159 out of an *FLC* mis-expression screen and exhibited late flowering shows the RNA-binding activity is
160 important for FCA function (Fig. EV1E). The impact of this missense mutation on the reduction of
161 RNA-binding activity was established through *in vitro* RNA-binding assays (Fig. EV1F).
162
163 To examine whether this RRM mutation affects FCA condensation, we generated transgene constructs
164 expressing an FCA wild-type genomic DNA fragment, with (FCArrm) and without (FCAwt) the
165 mutation fused with mScarlet-I and introduced them into *fca-9* mutant (Fig. EV1A). After selecting for
166 single insertion transgenic plants and homozygotes, we analysed the FCAwt condensates within the
167 nuclei of young roots using an Airyscan confocal microscope. The FCArrm transgene produced smaller,
168 more diffuse condensates at lower numbers, compared to wild type (Fig. 3A and B).
169
170 We also conducted single particle tracking with the FCArrm lines and observed the major oligomer
171 peak was slightly higher than that for FCAwt (Fig. 3C; Appendix Fig. S3). FCArrm particles with more
172 than 16 molecules were scarce, however, the integrated nuclear intensity of fluorescent signal in
173 FCArrm and FCAwt showed no obvious change (Appendix Fig. S4). This result suggests that the
174 reduced RNA-binding activity of FCA proteins decreases their likelihood of forming the larger particles
175 in the range of 16 to 56 molecules. We also compared the diffusion coefficients of individual particles
176 with their stoichiometry (Fig. 3D). The mean stoichiometry of FCArrm was lower than that of FCAwt,
177 while the overall the diffusion coefficients were slightly higher (Fig 3E; Appendix Fig. S5), however,
178 the periodic unit was not significantly changed (Fig. 3F). Thus, the RNA-binding activity of FCA
179 proteins affects multimerization of the FCA particles, and formation of the larger condensates, but does
180 not affect core oligomer assembly.
181
182 **The functional RNA-binding domain is required for *COOLAIR* R-loop resolution and FCA auto-**
183 **regulation.**

184 We then used the FCAwt and FCArrm lines to further investigate the functional importance of the RNA-
185 binding domain. Compared to the FCAwt transgenic plants, FCArrm plants displayed higher levels of
186 *FLC* expression and therefore flowered late (Fig. 4A and B, EV1B). FCA associates with *COOLAIR*,
187 recruiting 3' processing factors to promote proximal *COOLAIR* polyadenylation, thus resolving a
188 *COOLAIR*-formed R-loop (Liu et al, 2010; Xu et al, 2021). The ratio of proximal-to-distal isoforms of
189 *COOLAIR* transcripts was reduced in the FCArrm lines compared to FCAwt (Fig. 4C). Consistent with
190 this result, S9.6-DNA/RNA immunoprecipitation followed by cDNA conversion (DRIPc)-qPCR
191 analysis showed higher R-loop level in FCArrm relative to FCAwt, indicating that FCArrm has reduced
192 ability to resolve the *COOLAIR*-induced R-loop (Fig. 4D).
193
194 FCA autoregulates itself promoting polyadenylation at the proximal sites in intron 3 (Quesada et al,
195 2003), so we conducted Quant-seq analysis (Moll et al, 2014) to capture polyadenylated *FCA* transcripts
196 in Col-0, FCAwt, FCArrm and *fca-9.* In FCArrm and *fca-9*, there were significantly fewer reads
197 corresponding to proximally polyadenylated *FCA* transcripts compared to FCAwt and Col-0.
198 Conversely, reads at the distally polyadenylated site of *FCA* increased (Fig. 5), all consistent with
199 reduced FCA function. RNA-binding activity is thus important for FCA particle multimerization and
200 formation of the condensates, and for the well-defined FCA functional roles; promotion of proximal
201 *FCA* and *COOLAIR* termination and R-loop resolution.
202
203 **Discussion**
204 Our study provides insight on the functional properties of the dynamic liquid-like RNA 3' processing
205 condensates containing the Arabidopsis nuclear RNA-binding protein FCA. We conducted single
206 particle tracking to characterize molecular stoichiometry and diffusivity and the influence of protein
207 and RNA partners that function in *FLC* repression. Our work points to a modular structure for FCA
208 condensates centred around a low-order core oligomer, which multimerize to oligomers and
209 macromolecular condensates via associated RNA and FLL2 interaction. The genetic data support a
210 requirement for these condensates in FCA function for RNA 3' processing (Fig. 3A, 4 and EV4A; Fang
211 et al, 2019) with RNA-protein and protein-protein interactions playing different roles in the
212 oligomerization and condensation processes.
213
214 The FCA protein has many domains including an extended prion-like domain (Chakrabortee et al, 2016),
215 two RRM domains (Macknight et al, 1997), interrupted by a WW domain (Simpson et al, 2003;
216 Henderson et al, 2005) and an extended NH2 terminus that initiates translation with a CTG (non-
217 methionine) start codon (Simpson et al, 2010). Further work will be required to fully determine how all
218 these domains influence FCA condensate dynamics. Notably, the FCA core modular structure is
219 reminiscent of ELAV, a well-characterized Drosophila RNA-binding protein. ELAV with three RRM
220 domains tetramerizes on its target RNAs (Soller & White, 2005). For FCA condensates, the role of RNA

may involve functionality of the hydrophobic core in the RRM domain. The missense mutation (L304F) could strengthen the hydrophobic core in the FCA second RRM domain, an equivalent hydrophobic region to that recently found to influence the protein stability of TDP-43, an amyotrophic lateral sclerosis (ALS)-linked RNA binding protein (Mackness et al, 2024). RNA methylation may also be a contributing factor to the condensation dynamics as m6A has been shown to function in the regulatory mechanisms of *FLC* and *COOLAIR* (Xu et al, 2021; Wang et al, 2022; Sun et al, 2022; Amara et al, 2023).

COOLAIR transcription is enhanced upon cold exposure, and the transcripts form dense 'clouds' at each *FLC* locus, as judged by single-molecule RNA fluorescence in situ hybridization (Rosa et al, 2016). Whether the FCA condensates associate with these *COOLAIR* clouds will require RNA live imaging analysis. It is interesting to speculate that *COOLAIR* molecules might undergo thermo-responsive phase transitions as has been found recently for other RNAs (Wadsworth et al, 2023), with protein partners tuning this phase behaviour (Ruff et al, 2020). The *FLC* biological system has a lot of potential to uncover fundamental principles of condensate functionality *in vivo,* especially if we can successfully image the condensates at the locus. In mammalian cells, Mediator condensates only sporadically co-localize with *Sox2*, and this variability is attributed to a dynamic kissing model, where a Mediator condensate interacts with the gene only at specific timepoints (Cho et al, 2018; Du et al, 2024). This may be the case for *FLC,* which can exist in either a transcriptionally active (with functional FRIGIDA) or inactive (without functional FRIGIDA) state; with switching between these states connected to co-transcriptional RNA processing (Fang et al, 2020; Mateo-Bonmati et al, 2024; Menon et al, 2024). Exploring whether the transient association of FCA condensates with *FLC* locus reflects the transcriptional status of *FLC* will be the next important question.

In this study, we used SlimVar microscopy, which integrates Slimfield's technical capabilities with enhanced imaging contrast from variable-angle laser excitation (Plank et al, 2009; Payne-Dwyer et al, 2024). In contrast to a previous approach using a combination of Airyscan and Slimfield to infer the stoichiometry of FCA assemblies indirectly (Payne-Dwyer et al, 2022), SlimVar allowed for direct and precise single particle tracking and stoichiometric quantification of molecular assemblies in plant root tissue. The oblique excitation beam reduces out-of-focus background fluorescence, similar to HILO and lightsheet microscopy, and the use of an oil immersion objective lens improves fluorescence signal despite some optical aberration (Tokunaga et al, 2008; Stelzer et al, 2021). SlimVar calibration techniques such as adjusting the objective lens correction collar helped minimize these aberrations, enabling effective postprocessing "sifting" to collect robust signals (Payne-Dwyer et al, 2024). The limitations of SlimVar microscopy when observing FCA particles included the typically small field of view, which usually captures just one nucleus per acquisition. Additionally, the methodology suffered from fewer or shortened tracks due to bleaching, diffusion of assemblies, and residual aberration and

258 scattering, necessitating large sample numbers. Furthermore, at higher assembly concentrations, careful
259 image analysis was required to avoid overlapping assemblies leading to incorrect stoichiometry
260 estimates. Despite these limitations, SlimVar provides the ability to functionally study particles
261 involved in biomolecular condensation in Arabidopsis. This opens up the possibility of combining a
262 genetically tractable system with dissection of condensate function and their dynamic responses to
263 various environmental exposures.
264
265 **Methods**
266
267 **Plant materials and growth conditions**
268 The wild type Col-0, *fca-9* mutant allele, *pFCA::FCA-mTurquoise* and *pFLL2::FLL2-eYFP* transgenic
269 plants were described previously (Fang et al, 2019; Xu et al, 2021). To generate the *pFCA::FCA-*
270 *mScarlet-I* transgenic plants, the FCA genomic DNA fragment was amplified and inserted into the
271 pENTR vector. The mScarlet-I coding sequence was inserted before the stop codon via In-Fusion
272 seamless cloning. The FCA genomic DNA fragment fused mScarlet-I was transferred to pSLJ755I5
273 vector (Jones et al, 1992) via gateway cloning. The RRM mutation construct is modified from wild-
274 type FCA genomic DNA constructs via In-Fusion seamless cloning. Primers were listed in Table EV1.
275 These constructs were transformed into the *fca-9* mutant. Arabidopsis seeds were surface sterilized and
276 sown on standard Murashige and Skoog (MS) medium plate without glucose and stratified at 4 °C for
277 3 days before transferred to long-day conditions (16-h light at 20 °C, 8-h darkness at 16 °C) for 4-7
278 days.
279
280 **Confocal microscopy of FCA-mScarlet-I**
281 Confocal images were acquired on a Zeiss LSM 880 upright microscope equipped with an Airyscan
282 detector. Samples were imaged through a C-Apochromat 63x/NA 1.2 water-immersion objective by
283 exciting them at 561 nm and using the Airyscan detector in super resolution mode. The fluorescence
284 emission arrived at the detector after passing through a filter that allowed wavelengths between 495-
285 550 nm and above 570 nm to pass through. Typically, the voxel size was 0.06 × 0.06 × 0.26 µm (xyz)
286 and the pixel dwell time was 1.78 µs. Z-stacks typically comprised 28 slices and spanned a 7.13 µm
287 range for more than 70% of the nucleus. In Fig. 3A, the FCA-mScarlet-I signal was enhanced by shifting
288 its dynamic range to 0–160, and the images were processed using maximum intensity projection. After
289 Airyscan processing, the image analysis was performed in Arivis Vision4D ver. 4.1.0. (Zeiss). The blob
290 finder algorithm was applied to the mScarlet-I channel using a diameter value of 0.35 µm, a probability
291 threshold of 45%, and a split sensitivity of 50%. Blob finder is a segmentation algorithm that excels at
292 finding round or spherical objects in 2D or 3D, respectively. It uses a Gaussian scale to identify seeds
293 for the objects and subsequently applies a watershed algorithm to determine the boundaries of the
294 objects. To exclude non-specific identified condensates, a minimum size of 0.03 μm^3 and a sphericity
295 (Mesh) of 0.6 were set during the analysis, and non-specific foci outside the nuclear region of interest

were removed. Violin plots reflecting the data distribution were produced with GraphPad Prism 10 software.

Co-localization analysis of FCA and FLL2

Confocal images were acquired either on the Zeiss LSM 880 microscope mentioned above or a Zeiss LSM 980 confocal microscope. When using the LSM880, line by line sequential acquisition was employed. Samples were imaged through a C-Apochromat 63x/NA 1.2 water-immersion objective and were excited at 458 nm (mTurquoise) and 514 nm (eYFP). The fluorescence emission of the samples passed through a filter that only allowed wavelengths in the 465-505 nm range and above 525 nm to reach the Airyscan detector, which was operating in super resolution mode. The voxel size was 0.05 × 0.05 × 0.21 µm (xyz) and the pixel dwell time was 0.72 µs. Z-stacks comprised 25 slices spanning a 4.96 µm range. 0.2 µm TetraSpeck microspheres (Thermo Fisher Scientific) were imaged using these same settings and the resulting images were used to correct the sample images for chromatic aberration. The correction was performed in Zen (Zeiss) using the channel alignment method. In Fig. 2A, FCA-mTurquoise and FLL2-eYFP signal was enhanced by shifting the dynamic range of the signal to 0–1650 and 0-750.

After Airyscan processing, channel alignment, and nuclei segmentation, the image analysis was performed in Arivis Vision4D ver. 4.1.0. (Zeiss). Firstly, the blob finder algorithm was applied to the mTurquoise channel using a diameter value of 0.3 µm, a probability threshold of 37%, and a split sensitivity of 50%. Then, the blob finder algorithm was applied to the eYFP channel using a diameter value of 0.35 µm, a probability threshold of 37%, and a split sensitivity of 50%. Afterwards, the intersection between the output of the two blob finder operations was calculated. Finally, metrics such as volume, mean intensity, and total intensity were computed for the objects generated by each of the blob finder operations, as well as for their intersection. In general, a minimum size of 0.03 μm^3 and a sphericity (Mesh) of 0.6 were set during the analysis, and non-specific foci outside the nuclear region of interest were removed. Violin plots and x-y plots reflecting the data distribution were produced with GraphPad Prism 10 software.

SlimVar microscopy

For all imaging modalities, seedlings' root tips were oriented horizontally on slides containing MS media with 1% agarose, sealed with MS media under a No. 1.5 coverslip. The customized SlimVar microscope was previously described (Payne-Dwyer et al, 2024). Continuous wave lasers (Coherent OBIS) delivered a de-expanded Gaussian beam mode (TEM_{00}) to the back aperture of an NA 1.49 Apo TIRF 100× oil immersion objective lens (Nikon) with a lateral displacement such that the beam illuminated a sample area no greater than 9 × 16 µm at 60 ± 5º incidence. Single molecule sensitivity was achieved using a fast sCMOS camera (Photometrics Prime95B) which triggered a continuous wave laser for 10 ms exposure per frame at 80 Hz, providing optimal contrast for detection (Appendix Fig.

S6). The total magnification was approximately 200×, resulting in an oversampled image pixel edge size of 53 nm. Excitation and emission filters were tailored to best contrast for mScarlet-I (594/25 nm). Fluorescence acquisition settings in the red and complementary green channels were optimized to prevent initial saturation and to ensure the detection of individual molecular brightness tracks for mScarlet-I. To calibrate SlimVar, the beam displacement lens and objective lens correction collar were adjusted in situ to minimise optical aberrations at a representative 20 μm depth. These settings were then locked to prevent systematic variation in the characteristic single molecule brightness. Individual nuclei in the outermost 3 cell layers were identified in brightfield mode to determine the best focus without bleaching, and subsequently imaged in the SlimVar fluorescence mode until completely photobleached. Videos were subject to a temporal bleach correction (Fiji, Schindelin et al, 2012). Gaussian smoothing of 0.5 pixels (Fiji) were used on images, min/max adjusted for contrast, and the black point set at the background level outside the nucleus.

Single particle tracking and intensity analysis

Fluorescent particles were identified from SlimVar image sequences and linked into tracks using ADEMScode software (Plank et al, 2009) using a strict 'sifting' approach. This sets signal-to-noise and distance thresholds to discard foci with low contrast, whose integrated intensity is influenced by background or detection noise, or exhibit nonphysical mobility. Each of these particles were localised to a super-resolved, subpixel precision, typically 40 nm. The random overlap probability was estimated using a nearest neighbour distance approach as <5% for all observed tracks (Payne-Dwyer et al, 2024). Analysis was spatially restricted to data lying within a region of effectively uniform laser illumination (80% ± 9% s.d. peak intensity) by cropping images to an area of 240 × 184 pixels (12.7 × 9.8 μm). Fluorescence image sequences were further cropped to specify individual nuclei, using manually segmented masks from brightfield images.

The 2D diffusion coefficient of each track (D) was computed using the increase of mean-square displacement across time interval according to a random walk model (Leake et al, 2008). Focus intensity was calculated by summing the pixel values within a 5-pixel distance and subtracting an averaged background level from the rest of a 17-pixel square (Leake et al, 2008). The track stoichiometry was found by extrapolating the particle's intensity in the first 5 image frames s to account for photobleaching (Syeda et al, 2019), then dividing this initial intensity by the characteristic single molecule brightness (Wollman et al, 2017). The characteristic single molecule brightness linked to each reporter was determined as 110 ± 15 (mean ± s.d.) for mScarlet-I based on the modal size of steps in track intensity during late-stage photobleaching. The track intensities over time were first denoised using an edge preserving filter (Chung and Kennedy, 1991). This characteristic single molecule brightness provides an internal calibration for track stoichiometry, periodicity, and integrated nuclear intensity which is refined to nuclear protein number.

370 To calculate periodicity, the stoichiometries of all tracks within each nucleus were represented as a
371 kernel density distribution (Leake et al, 2014), employing an empirical standard deviation of 0.6
372 molecules on the characteristic single molecule brightness. Peaks within this distribution were identified
373 using the MATLAB *findpeaks* function, and the intervals between nearest neighbour peaks were
374 computed (Payne-Dwyer et al, 2024). Raw estimations of the total number of molecules in each nucleus
375 were determined using ImageJ macros to integrate the pixel values inside segmented nuclei as in
376 previous work (Wollman & Leake, 2015; Payne-Dwyer et al, 2024). The nuclear protein number of
377 each reporter dataset was refined to exclude autofluorescence by calculating the difference between
378 mean integrated nuclear intensities of the labelled dataset and an unlabeled control, adjusted
379 proportionally to the ratio of mean nuclear segment areas.
380
381 ***In vitro* protein expression and purification**
382 MBP-RRM and MBP-PrLD proteins were expressed and purified from *Escherichia coli* (Rosetta) cells
383 using Ni-NTA resin as described previously (Fang et al, 2019). Briefly, protein expression was induced
384 by 0.4 mM isopropyl-β-D-1-thiogalactopyranoside (IPTG) at 18°C overnight. Cells were collected by
385 centrifugation and re-suspended in lysis buffer (40 mM Tris-HCl pH7.4, 500 mM NaCl, 10% glycerol).
386 The suspension was sonicated for 20 min (3 s ON, 3 s OFF, SCIENTZ) and centrifuged at 13000 *g* for
387 30 min at 4°C. The supernatant was incubated with Ni-NTA agarose for 20 min, washed and eluted with
388 buffer E (40 mM Tris-HCl pH7.4, 500 mM NaCl, 500 mM Imidazole, Sangon). Proteins were further
389 purified by gel filtration chromatography (Superdex-200; GE Healthcare) and stored in buffer S (40
390 mM Tris-HCl pH7.4, 500 mM NaCl, 1 mM DTT) at −80 °C.
391
392 **Size-exclusion chromatography coupled with multi-angle laser light scattering (SEC-MALS)**
393 Multi-angle light scattering experiments were performed in 40 mM Tris-HCl pH7.4 and 500 mM NaCl
394 using a Superdex-200 10/300 GL size exclusion column (GE Healthcare). The concentration of MBP-
395 RRM and MBP-PrLD used was 2 mg/mL. The chromatography system was connected to a Wyatt
396 DAWN HELEOS laser photometer and a Wyatt Optilab T-rEX differential refractometer. Wyatt ASTRA
397 7.3.2 software was used for data analysis.
398
399 **Expression analysis**
400 Total RNA was extracted from plant materials as described previously (Qüesta et al, 2016), treated with
401 TURBO DNase (Thermo Fisher Scientific) to eliminate DNA contamination, and reverse-transcribed
402 using SuperScript IV Reverse Transcriptase (Thermo Fisher Scientific) with gene-specific reverse
403 primers. Quantitative PCR (qPCR) analysis was conducted on a LightCycler480 II (Roche), and the
404 qPCR data were normalized to the reference genes *UBC*. To measure the proximal ratio of *COOLAIR*,
405 the level of the proximal component was normalized to the distal *COOLAIR*. Primers were listed in
406 Table EV1.

407

408 **DNA−RNA hybrid immunoprecipitation followed by cDNA conversion (DRIPc)**

409 The DRIP protocol is as described previously (Xu et al, 2021) with modifications. In general, 3 g 10-
410 day-old seedlings were harvested and grounded into a fine powder. The powder was suspended in 35
411 mL of Honda buffer (20mM HEPES, 0.44M sucrose, 1.25% Ficoll, 2.5% dextran T40, 10mM $MgCl_2$,
412 0.5% Triton x-100, 5 mM DTT, 1x protease inhibitor cocktail (Roche), filtered through one layer of
413 Miracloth, and centrifuged at 3500×g for 15 min. Nuclear pellets were resuspended in 1mL Honda
414 buffer and centrifuged at 8000×g for 1 min. Pellets were then resuspended in the lysis buffer (50mM
415 Tris-HCl pH 8.0, 10mM EDTA, 1% SDS) supplied with 0.1 mg/mL proteinase K (AM2546, Thermo
416 Fisher Scientific) and digested at 55 °C overnight with gentle rotation. The mixture was
417 phenol/chloroform extracted, followed by nucleic acid precipitation with NaOAc and ethanol. The
418 nucleic acid pellet was dissolved in water and quantified with Qubit DNA quantification kit (Thermo
419 Fisher Scientific). In general, 1 μg of nucleic acid was digested by restriction enzymes including DdeI,
420 NdeI and XbaI (NEB) overnight. The digested nucleic acid was phenol/chloroform extracted, followed
421 by nucleic acid precipitation with NaOAc and ethanol. Then the nucleic acid was treated with RNAse
422 III (Thermo Fisher Scientific) and then extracted by phenol/chloroform and ethanol precipitation. The
423 treated nucleic acid was then diluted ten times with dilution buffer (16.7mM Tris pH 7.5, 167mM NaCl,
424 2.2mM EDTA, 0.1% Triton X-100) and 10% was stored at −20 °C as input. In all, 5 μg of S9.6 antibody
425 (1:100 dilution, ENH001, Kerafast) was added, then incubated overnight at 4 °C. The next day, 50 μl
426 Dynabeads Protein G (Thermo Fisher Scientific) was added and incubated for another 2 h. The
427 immunoprecipitants were washed five times with dilution buffer and twice with TE buffer, then were
428 eluted in 100 μl elution buffer (10mM Tris pH 7.5, 2 mM EDTA, 0.2% SDS, 100 ng/μl tRNA) and 5 μl
429 proteinase K at 55 °C for 2 hours, together with input samples. The nucleic acids were precipitated with
430 NaOAc, isopropanol, and glycogen, dissolved in water. The DRIP nucleic acid samples were then
431 treated with TURBO DNase (Thermo Fisher Scientific) to eliminate DNA contamination, and reverse-
432 transcribed using SuperScript IV Reverse Transcriptase (Thermo Fisher Scientific) with gene-specific
433 reverse primers. All the samples including inputs were subjected to qPCR analysis via LightCycler480
434 II (Roche). The data were normalized to 1% of input. Primers were listed in Table EV1.

435

436 **Quant-seq**

437 The Quant-seq protocol is as described previously (Mateo-Bonmatí et al, 2024). The total RNAs
438 prepared for Quant-seq underwent purification using the Qiagen RNeasy miniprep kit (QIAGEN,
439 74106). Lexogen GmbH (Austria) conducted the library preparation, sequencing, and data analysis.
440 Sequencing-ready libraries were created from 100 ng of input RNA using a QuantSeq 3' mRNA-Seq
441 Library Prep Kit REV for Illumina (015UG009V0271), following standard procedures. The RNA
442 integrity and quality of indexed libraries were assessed on a Fragment Analyzer device (Agilent
443 Technologies) using a DNF-471 RNA Kit and HS-DNA assay, respectively. Library quantification was

444 carried out using a Qubit dsDNA HS assay (Thermo Fisher Scientific). A sequencing-ready pool of
445 indexed libraries was then sequenced on an Illumina NextSeq 2000 with a 100-cycle cartridge, using
446 the Custom Sequencing Primer (CSP). Verification of read quality utilized FastQC version v0.11.7, and
447 read adapter trimming employed cutadapt version 1.18 (Martin, 2011). Clean reads were mapped to the
448 latest version of the Arabidopsis genome (TAIR10) using the splice-aware aligner STAR version 2.6.1a
449 (Dobin et al, 2013).
450
451 **Electrophoretic Mobility Shift Assay**
452 FCA cDNA with L304F mutation was amplified from the mutant as described in Fig. EV1.
453 To generate RNA probes, dsDNA of the corresponding region was amplified through PCR (primers see
454 Table EV1) with the T7/T3 phage polymerase promoter added at the 5' end of the primer. *COOLAIR*
455 RNA was then generated by following a protocol provided by the MAXIscript® T7 Transcription Kit
456 (Thermo Fisher Scientific). The resulting product was DNA digested, denatured, and separated on 5%
457 TBE gel containing 8 M Urea. The band at the right size was cut out, sliced, and eluted in gel extraction
458 buffer (0.5 M NH_4Ac, 1 mM EDTA, 0.2% SDS, 1xRNAsecure (Thermo Fisher Scientific) at 37ºC
459 overnight, followed by precipitation with isopropanol. 10 pmol purified RNA was 3'biotinylated by
460 following the instructions provided by the RNA 3' End Biotinylation Kit (Thermo Fisher Scientific).
461 The labelling efficiency was determined to be at least 90%. For the gel shift assay, a 20 µl reaction (25
462 ng/µl protein, 2 nM probe, 250 ng/µl tRNA, 50 ng/µl heparin, 10 mM HEPES (pH 7.3), 120 mM KCL,
463 1 mM $MgCl_2$, 1 mM DTT) was set up on ice. For the competition assay, 2x to 100x of unlabelled probe
464 was included in the reaction. The reaction with only GST was used as a negative control. The mixture
465 was incubated at room temperature for 5 min and resolved on 3.5% native TBE-acrylamide gel and
466 transferred onto a positively charged nylon membrane. The biotinylated RNA on the membrane was
467 detected by chemiluminescence according to a protocol provided with the Chemiluminescent Nucleic
468 Acid Detection Module (Thermo Fisher Scientific, 89880). For the binding reaction, 1 µg of different
469 recombinant proteins was incubated with 2 pmol of biotinylated probe in 20 µL of 1× buffer containing
470 20 mM Tris (pH 7.5), 100 mM NaCl, 10 mM $MgCl_2$, non-specific competitors (1µg/µl heparin and 5µg
471 tRNA) and 0.05% Triton X-100 at room temperature for 10 min. The RNA-protein mixture was
472 resolved on 6% 1× TBE acrylamide gel under 100 V for 50 min, followed by electrophoretic transfer
473 to positively charged nylon membranes (GE Healthcare). The biotinylated RNA on the membrane was
474 UV cross-linked and detected using chemiluminescent nucleic acid detection following the
475 manufacturer's instructions (Thermo Fisher Scientific).
476
477 **Data availability**
478 Raw image data of confocal microscopy and co-localization analysis have been deposited in the
479 BioImage Archive (https://www.ebi.ac.uk/biostudies/bioimages/studies/S-BIAD1154). The raw and
480 processed imaging data and analysed tracks of single particle tracking analysis are available at the

BioStudies: https://doi.org/10.6019/S-BIAD1234. The ADEMScode MATLAB tracking analysis software can be found at https://github.com/alex-payne-dwyer/single-molecule-tools-alpd. The raw reads of Quant-seq have been deposited in the Short Read Archive (SRA) under the reference (PRJNA1087342 and PRJNA1076161).

Acknowledgements

We thank Shuqin Chen, Tina Zhang, JIC Horticultural Services and JIC Bioimaging facility for their excellent technical assistance and Hsuan Pai (TSL) for her artwork assistance. We thank Simon H. Stitzinger and Jose A. M. Lantero (MPI-IE) for helpful discussion. We also thank all members of the Caroline Dean and Martin Howard groups. This work was funded by the European Research Council Advanced Grant (EPISWITCH, 833254), Wellcome Trust (210654/Z/18/Z), and the Royal Society Professorship (RSRP\R\231006) to Caroline Dean, and EPSRC grants (EP/T00214X/1 to C.D. and EP/T002166/1 and EP/W024063/1 to M.L).

Disclosure and competing interest statement

The authors declare that they have no conflict of interest.

References

Amara U, Hu J, Cai J & Kang H (2023) FLK is an mRNA m6A reader that regulates floral transition by modulating the stability and splicing of *FLC* in Arabidopsis. *Mol Plant* 16: 919–929

Banani SF, Lee HO, Hyman AA & Rosen MK (2017) Biomolecular condensates: Organizers of cellular biochemistry. *Nat. Rev. Mol. Cell Biol.* 18: 285-298

Bienz M (2020) Head-to-tail polymerization in the assembly of biomolecular condensates. *Cell* 182: 799–811

Bayle V, Fiche JB, Burny C, Platre MP, Nollmann M, Martinière A & Jaillais Y (2021) Single-particle tracking photoactivated localization microscopy of membrane proteins in living plant tissues. *Nat Protoc* 16: 1600–1628

Berry S, Rosa S, Howard M, Bühler M & Dean C (2017) Disruption of an RNA-binding hinge region abolishes LHP1-mediated epigenetic repression. *Genes Dev* 31: 2115–2120

Bindels DS, Haarbosch L, Van Weeren L, Postma M, Wiese KE, Mastop M, Aumonier S, Gotthard G, Royant A, Hink MA *et al* (2016) mScarlet: A bright monomeric red fluorescent protein for cellular imaging. *Nat Methods* 14: 53–56

Biswas S, Chen Z, Karslake JD, Farhat A, Ames A, Raiymbek G, Freddolino PL, Biteen JS & Ragunathan K (2022) HP1 oligomerization compensates for low-affinity H3K9me recognition and provides a tunable mechanism for heterochromatin-specific localization. *Sci Adv* 8

Chakrabortee S, Kayatekin C, Newby GA, Mendillo ML, Lancaster A & Lindquist S (2016) Luminidependens (LD) is an Arabidopsis protein with prion behavior. *Proc Natl Acad Sci U S A* 113: 6065–6070

Cho WK, Spille JH, Hecht M, Lee C, Li C, Grube V & Cisse II (2018) Mediator and RNA polymerase II clusters associate in transcription-dependent condensates. *Science* 361: 412–415

Chung SH & Kennedy RA (1991) Forward-backward non-linear filtering technique for extracting small biological signals from noise. *J Neurosci Methods* 40: 71–86

Dobin A, Davis CA, Schlesinger F, Drenkow J, Zaleski C, Jha S, Batut P, Chaisson M & Gingeras TR (2013) STAR: Ultrafast universal RNA-seq aligner. *Bioinformatics* 29: 15–21

Du M, Stitzinger SH, Spille J, Hijaz M, Quintana A, Cisse II, Du M, Stitzinger SH, Spille J, Cho W *et al* (2024) Direct observation of a condensate effect on super- enhancer controlled gene bursting.

527 *Cell* 187: 331–344
528 Fang X, Wang L, Ishikawa R, Li Y, Fiedler M, Liu F, Calder G, Rowan B, Weigel D, Li P *et al*
529 (2019) Arabidopsis FLL2 promotes liquid–liquid phase separation of polyadenylation complexes.
530 *Nature* 569: 265–269
531 Fang X, Wu Z, Raitskin O, Webb K, Voigt P, Lu T, Howard M & Dean C (2020) The 3' processing of
532 antisense RNAs physically links to chromatin-based transcriptional control. *Proc Natl Acad Sci U*
533 *S A* 117: 15316–15321
534 Fiedler M, Franco-Echevarría E, Schulten A, Nielsen M, Rutherford TJ, Yeates A, Ahsan B, Dean C
535 & Bienz M (2022) Head-to-tail polymerization by VEL proteins underpins cold-induced Polycomb
536 silencing in flowering control. *Cell Rep* 41
537 Field S, Jang GJ, Dean C, Strader LC & Rhee SY (2023) Plants use molecular mechanisms mediated
538 by biomolecular condensates to integrate environmental cues with development. *Plant Cell* 35:
539 3173–3186
540 Henderson IR, Liu F, Drea S, Simpson GG & Dean C (2005) An allelic series reveals essential roles
541 for FY in plant development in addition to flowering-time control. *Development* 132: 3597–3607
542 Izeddin I, Récamier V, Bosanac L, Cissé II, Boudarene L, Dugast-Darzacq C, Proux F, Bénichou O,
543 Voituriez R, Bensaude O *et al* (2014) Single-molecule tracking in live cells reveals distinct target-
544 search strategies of transcription factors in the nucleus. *Elife* 3: 1–27
545 Jin X, Lee JE, Schaefer C, Luo X, Wollman AJM, Payne-Dwyer AL, Tian T, Zhang X, Chen X, Li Y,
546 *et al* (2021) Membraneless organelles formed by liquid-liquid phase separation increase bacterial
547 fitness. *Sci Adv* 7
548 Jones JDG, Shlumukov L, Carland F, English J, Scofield SR, Bishop GJ & Harrison K (1992)
549 Effective vectors for transformation, expression of heterologous genes, and assaying transposon
550 excision in transgenic plants. *Transgenic Res.* 1: 285–297
551 Jumper J, Evans R, Pritzel A, Green T, Figurnov M, Ronneberger O, Tunyasuvunakool K, Bates R,
552 Žídek A, Potapenko A *et al* (2021) Highly accurate protein structure prediction with AlphaFold.
553 *Nature* 596: 583–589
554 Kent S, Brown K, Yang C hsun, Alsaihati N, Tian C, Wang H & Ren X (2020) Phase-separated
555 transcriptional condensates accelerate target-search process revealed by live-cell single-molecule
556 imaging. *Cell Rep* 33: 108248
557 Ladouceur AM, Parmar BS, Biedzinski S, Wall J, Tope SG, Cohn D, Kim A, Soubry N, Reyes-
558 Lamothe R & Weber SC (2020) Clusters of bacterial RNA polymerase are biomolecular
559 condensates that assemble through liquid-liquid phase separation. *Proc Natl Acad Sci U S A* 117:
560 18540–18549
561 Leake MC, Chandler JH, Wadhams GH, Bai F, Berry RM & Armitage JP (2006) Stoichiometry and
562 turnover in single, functioning membrane protein complexes. *Nature* 443: 355–358
563 Leake MC, Greene NP, Godun RM, Granjon T, Buchanan G, Chen S, Berry RM, Palmer T & Berks
564 BC (2008) Variable stoichiometry of the TatA component of the twin-arginine protein transport
565 system observed by in vivo single-molecule imaging. *Proc Natl Acad Sci U S A* 105: 15376–15381
566 Leake MC (2014) Analytical tools for single-molecule fluorescence imaging in cellulo. *Phys Chem*
567 *Chem Phys* 16: 12635–12647
568 Liu F, Quesada V, Crevillén P, Bäurle I, Swiezewski S & Dean C (2007) The Arabidopsis RNA-
569 Binding Protein FCA Requires a Lysine-Specific Demethylase 1 Homolog to Downregulate *FLC*.
570 *Mol Cell* 28: 398–407
571 Liu F, Marquardt S, Lister C, Swiezewski S & Dean C (2010) Targeted 3′ processing of antisense
572 transcripts triggers Arabidopsis *FLC* chromatin silencing. *Science* 327: 94-7
573 Mackness BC, Morgan BR, Deveau LM, Kathuria S V., Zitzewitz JA & Massi F (2024) A
574 hydrophobic core stabilizes the residual structure in the RRM2 intermediate state of the ALS-
575 linked protein TDP-43. *bioRxiv* 2024.06.12.598648.
576 Macknight R, Bancroft I, Page T, Lister C, Schmidt R, Love K, Westphal L, Murphy G, Sherson S,
577 Cobbett C *et al* (1997) FCA, a gene controlling flowering time in Arabidopsis, encodes a protein
578 containing RNA-binding domains. *Cell* 89: 737–745
579 Martin M (2011) Cutadapt removes adapter sequences from high-throughput sequencing reads.
580 *EMBnet.journal* 17: 10-12
581 Mateo-Bonmatí E, Montez M, Maple R, Fiedler M, Fang X, Saalbach G, Passmore LA & Dean C

582 (2024) A CPF-like phosphatase module links transcription termination to chromatin silencing. *Mol*
583 *Cell* 84: 2272–2286
584 Menon G, Mateo-Bonmati E, Reeck S, Maple R, Wu Z, Ietswaart R, Dean C & Howard M (2024)
585 Proximal termination generates a transcriptional state that determines the rate of establishment of
586 Polycomb silencing. *Mol Cell* 84: 2255–2271
587 Moll P, Ante M, Seitz A & Reda T (2014) QuantSeq 3' mRNA sequencing for RNA quantification.
588 *Nat Methods* 11: i–iii
589 Payne-Dwyer AL & Leake MC (2022) Single-molecular quantification of flowering control proteins
590 within nuclear condensates in live whole Arabidopsis root. *Methods Mol Biol.* 2476:311–328.
591 Payne-Dwyer AL, Jang GJ, Dean C & Leake MC (2024) SlimVar : rapid in vivo single-molecule
592 tracking of chromatin regulators in plants. bioRxiv 2024.05.17.594710.
593 Peran I & Mittag T (2020) Molecular structure in biomolecular condensates. *Curr Opin Struct Biol*
594 60: 17–26
595 Plank M, Wadhams GH & Leake MC (2009) Millisecond timescale slimfield imaging and automated
596 quantification of single fluorescent protein molecules for use in probing complex biological
597 processes. *Integr Biol* 1: 602–612
598 Quesada V, Macknight R, Dean C & Simpson GG (2003) Autoregulation of FCA pre-mRNA
599 processing controls Arabidopsis flowering time. *EMBO J* 22: 3142–3152
600 Qüesta JI, Song J, Geraldo N, An H & Dean C (2016) Arabidopsis transcriptional repressor VAL1
601 triggers Polycomb silencing at *FLC* during vernalization. *Science* 353: 485–488
602 Reyes-Lamothe R, Sherratt DJ & Leake MC (2010) Stoichiometry and architecture of active DNA
603 replication machinery in *Escherichia coli*. *Science* 328: 498–501
604 Rosa S, De Lucia F, Mylne JS, Zhu D, Ohmido N, Pendle A, Kato N, Shaw P & Dean C (2013)
605 Physical clustering of *FLC* alleles during polycomb-mediated epigenetic silencing in vernalization.
606 *Genes Dev* 27: 1845–1850
607 Rosa S, Duncan S & Dean C (2016) Mutually exclusive sense-antisense transcription at *FLC*
608 facilitates environmentally induced gene repression. *Nat Commun* 7: 1–7
609 Ruff KM, Dar F & Pappu R V. (2021) Ligand effects on phase separation of multivalent
610 macromolecules. *Proc Natl Acad Sci U S A* 118
611 Schindelin J, Arganda-Carreras I, Frise E, Kaynig V, Longair M, Pietzsch T, Preibisch S, Rueden C,
612 Saalfeld S, Schmid B *et al* (2012) Fiji: an open-source platform for biological-image analysis. *Nat*
613 *Methods* 9: 676–682
614 Shen Z, Jia B, Xu Y, Wessén J, Pal T, Chan HS, Du S & Zhang M (2023) Biological condensates
615 form percolated networks with molecular motion properties distinctly different from dilute
616 solutions. *Elife* 12: 1–32
617 Shin Y & Brangwynne CP (2017) Liquid phase condensation in cell physiology and disease. *Science*
618 357
619 Simpson GG, Dijkwel PP, Quesada V, Henderson I & Dean C (2003) FY is an RNA 3′ end-
620 processing factor that interacts with FCA to control the Arabidopsis floral transition. *Cell* 113:
621 777–787
622 Simpson GG, Laurie RE, Dijkwel PP, Quesada V, Stockwell PA, Dean C & Macknight RC (2010)
623 Noncanonical translation initiation of the Arabidopsis flowering time and alternative
624 polyadenylation regulator FCA. *Plant Cell* 22: 3764–3777
625 Soller M & White K (2005) ELAV multimerizes on conserved AU4-6 motifs important for *ewg*
626 splicing regulation. *Mol Cell Biol* 25: 7580–7591
627 Stelzer EHK, Strobl F, Chang B-J, Preusser F, Preibisch S, McDole K & Fiolka R (2021) Light sheet
628 fluorescence microscopy. *Nat Rev Methods Prim* 1: 73
629 Syeda AH, Wollman AJM, Hargreaves AL, Howard JAL, Bruning JG, McGlynn P & Leake MC
630 (2019) Single-molecule live cell imaging of Rep reveals the dynamic interplay between an
631 accessory replicative helicase and the replisome. *Nucleic Acids Res* 47: 6287–6298
632 Sun B, Bhati KK, Song P, Edwards A, Petri L, Kruusvee V, Blaakmeer A, Dolde U, Rodrigues V,
633 Straub D *et al* (2022) FIONA1-mediated methylation of the 3'UTR of *FLC* affects *FLC* transcript
634 levels and flowering in Arabidopsis. *PLoS Genet* 18: 1–22
635 Tokunaga M, Imamoto N & Sakata-Sogawa K (2008) Highly inclined thin illumination enables clear
636 single-molecule imaging in cells. *Nat Methods* 5: 159–161

Varadi M, Anyango S, Deshpande M, Nair S, Natassia C, Yordanova G, Yuan D, Stroe O, Wood G, Laydon A *et al* (2022) AlphaFold Protein Structure Database: Massively expanding the structural coverage of protein-sequence space with high-accuracy models. *Nucleic Acids Res* 50: D439–D444

Wang C, Yang J, Song P, Zhang W, Lu Q, Yu Q & Jia G (2022) FIONA1 is an RNA N 6-methyladenosine methyltransferase affecting Arabidopsis photomorphogenesis and flowering. *Genome Biol* 23: 1–29

Wadsworth GM, Zahurancik WJ, Zeng X, Pullara P, Lai LB, Sidharthan V, Pappu R V., Gopalan V & Banerjee PR (2023) RNAs undergo phase transitions with lower critical solution temperatures. *Nat Chem* 15: 1693–1704

Wollman AJM & Leake MC (2015) Millisecond single-molecule localization microscopy combined with convolution analysis and automated image segmentation to determine protein concentrations in complexly structured , functional cells , one cell at a time. *Faraday Discuss* 00: 1–24

Wollman AJM, Shashkova S, Hedlund EG, Friemann R, Hohmann S & Leake MC (2017) Transcription factor clusters regulate genes in eukaryotic cells. *Elife* 6: 1–36

Xu C, Wu Z, Duan HC, Fang X, Jia G & Dean C (2021) R-loop resolution promotes co-transcriptional chromatin silencing. *Nat Commun* 12, 1790

Zhu P, Lister C & Dean C (2021) Cold-induced Arabidopsis FRIGIDA nuclear condensates for *FLC* repression. *Nature* 599: 657–661

Table EV1: Primers

Primer name	**Primer sequence 5' -> 3'**	**Annotations**
Primers for cloning		
Inf-XhoI-pFCA-F	CGGGCCCCCCCTCGACGAGCGGTGAAGATGTATTGT	Cloning of FCA genomic fragments with Infusion strategy
Inf-BamHI-FCA-3UTR-R	TAGAACTAGTGGATCACAACCTTGAGTTCCTCGAGT	
Inf-FCA-stop-linear-R	AGCTTTATTCTTCCACATGAGTTCTTGG	
Inf-FCA-stop-linear-F	TGAGGTTCATATCTACCCTTTCTCTCCT	
Inf-FCA-linker-mScarletI-F	TGGAAGAATAAAGCTTCTGCTGCCGCATCCGCGGCAGCTTCAGCCGTGAGCAAGGGCGAGGCA	Cloning of FCA-mScarlet-I with Infusion strategy
Inf-FCA-mScarletI-R	TAGATATGAACCTCACTTGTACAGCTCGTCCATGC	
Inf-FCA-stop-linear-R	AGCTTTATTCTTCCACATGAGTTCTTGG	Cloning of FCA fusion protein with Infusion strategy
Inf-FCA-stop-linear-F	TGAGGTTCATATCTACCCTTTCTCTCCT	
Inf-NdeI-FCA-In3-F	TAGGTGGTGCAAACATATGGA	Cloning of L304F mutation on FCA fragments with Infusion strategy
Inf-FCA-L304F-R	AAAAAACTTAAACTCTAGGGTGC	
Inf-FCA-L304F-F	CCCTAGAGTTTAAGTTTTTTGTTGG	
Inf-AfeI-FCA-In6-R	GTAGAATGTCCAAGCGCTT	

Primers for transcript analyses		
FCAγ-qPCR-F	TCAGTCGTGCAACTGCTCCTC	Spliced *FCAγ* qPCR
FCAγ-qPCR-R	GATCCAGCCCACTGTTGTTT	
FLC spliced F	AGCCAAGAAGACCGAACTCA	Spliced *FLC* qPCR
FLC spliced R	TTTGTCCAGCAGGTGACATC	
Set1 new LP	TGGTTGTTATTTGGTGGTGTG	RT for proximal *COOLAIR*
set2_new_2_LP	CCTGCTGGACAAATCTCCGA	Proximal *COOLAIR* qPCR
set2_new_2_RP	TCACACGAATAAGGTGGCTAATTAAG	
FLC -158_F	GCCCGACGAAGAAAAAGTAG	RT for distal *COOLAIR*
Set4-new-F-195	GTATCTCCGGCGACTTGAAC	Distal *COOLAIR* qPCR
Set4-new-R-195	GGATGCGTCACAGAGAACAG	
UBC_qPCR_F	CTGCGACTCAGGGAATCTTCTAA	*UBC* qPCR
UBC_qPCR_R	TTGTGCCATTGAATTGAACCC	
Primers for DRIPc-qPCR		
4319f	AGAACAACCGTGCTGCTTTT	A
4466r	TGTGTGCAAGCTCGTTAAGC	
5030F	CCGGTTGTTGGACATAACTAGG	B
5153R	CCAAACCCAGACTTAACCAGAC	
5327f	TTTTTGTTATGGTTAGGTTTGGA	C
5395r	AGTAGCACTACTTCTAGACACTTGGA	
5456f	GCTTCCAAACTTAAAAGCTTAAACA	D
5584r	TCTTTTTGTCTTCTATCCAAGGAAT	
5531F	TGGTTGTTATTTGGTGGTGTG	E

5652R	CTGCTCCCACATGATGATTA	
Primers for EMSA		
FCA-EMSA-F1-718-T7	AAGTAATACGACTCACTATAGGGATTTCAACCGCCG ATTTAAG	
FCA-EMSA-R-T3	AAGAATTAACCCTCACTAAAGGGTTCCGGTTGTTG GACATAACT	

658

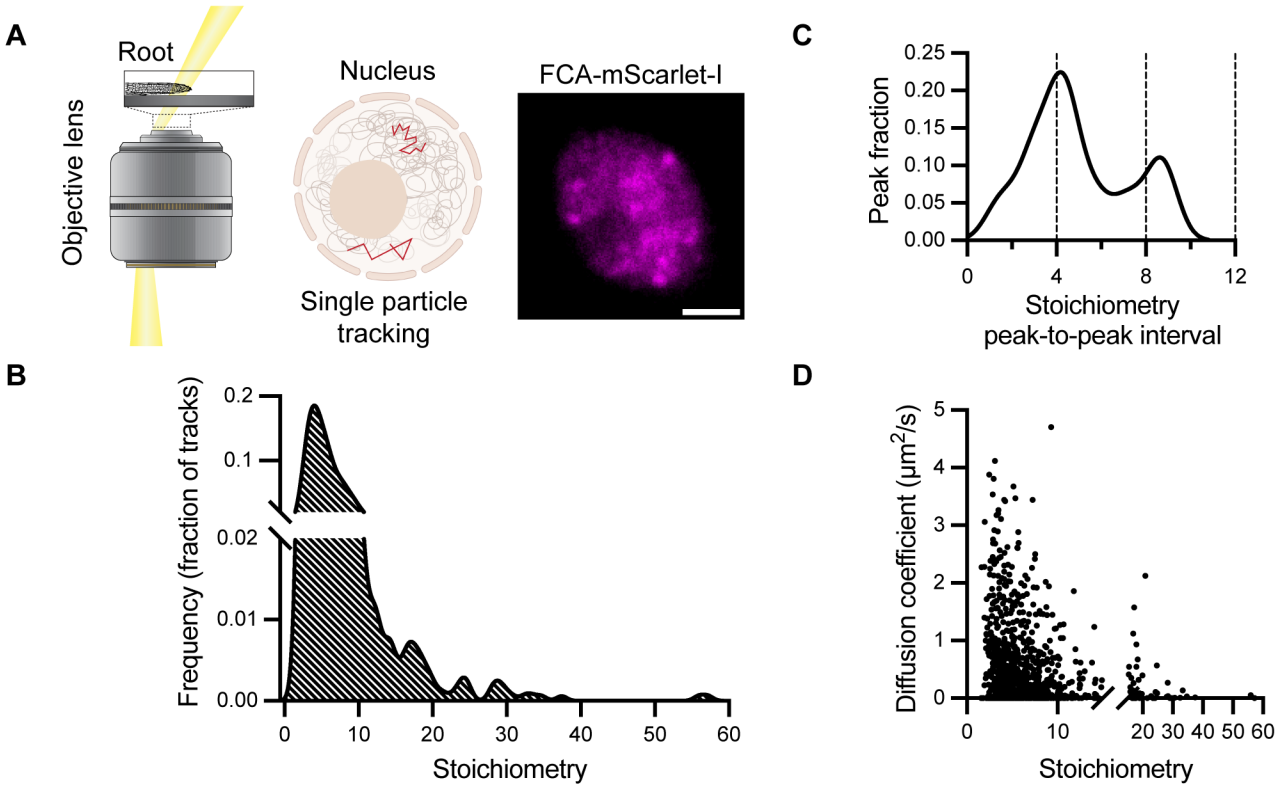

Figure 1. Super-resolution microscopy and single particle tracking to determine the physical characteristics of FCA particles
(**A**) A schematic of SlimVar microscopy used for the imaging Arabidopsis root cells and an example of a SlimVar image of a nucleus showing FCA-mScarlet-I (magenta). Scale bar: 2 μm. (**B**) Distribution of the stoichiometry (molecule number) of individual FCA particles. (**C**) Periodicity of FCA particle stoichiometry estimated from the most common spacing between neighboring peaks in each stoichiometry distribution. (**D**) The diffusion coefficient and stoichiometry of each FCA particle. The single particle tracking analysis is from three biologically independent experiments. Results from individual replicate are provided in Appendix Figure S3.

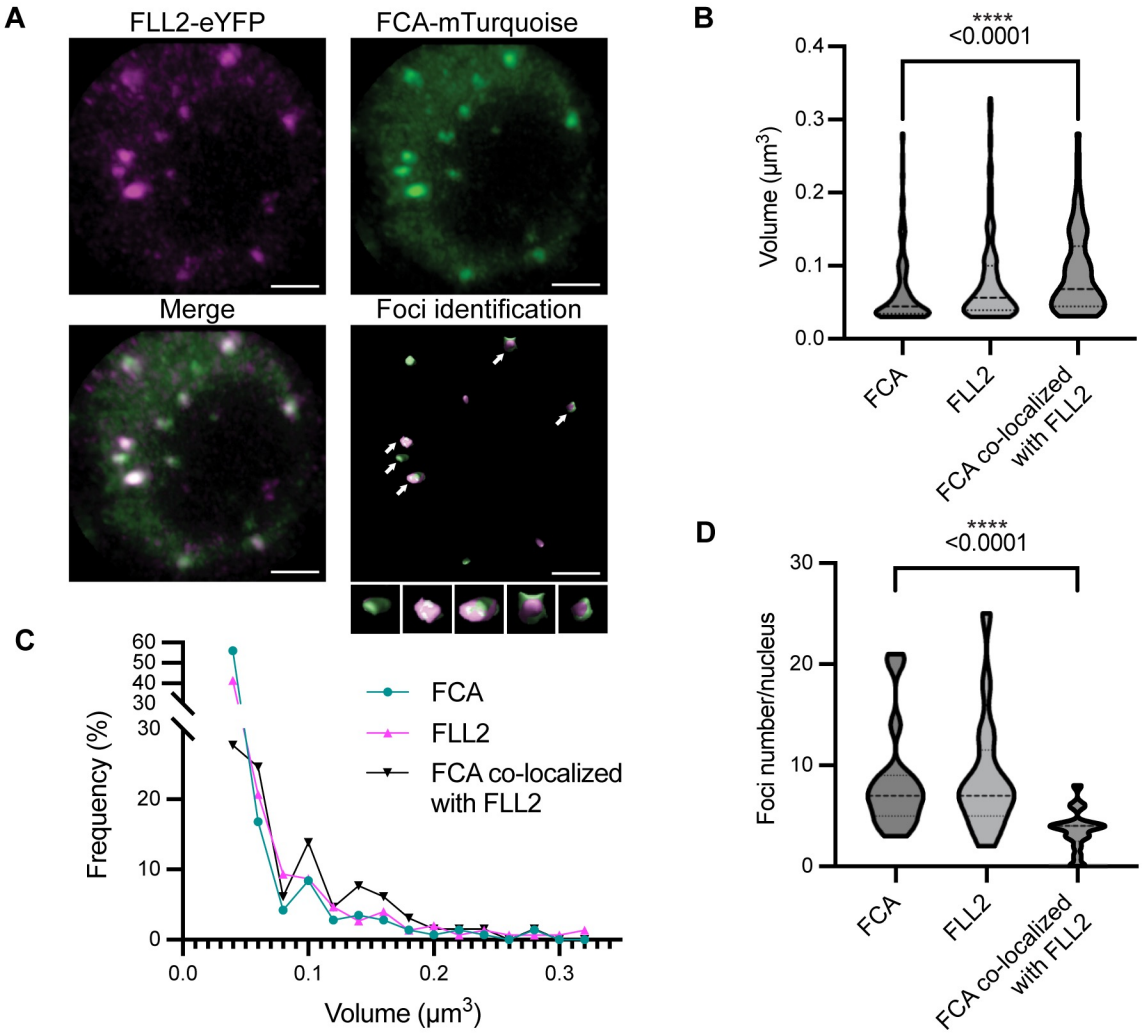

Figure 2. The co-localization of FCA and FLL2 is associated with larger sized condensates in Arabidopsis nuclei

(**A**) Selected 3D images of FCA and FLL2 colocalization. FCA-mTurquoise signal (green) and FLL2-eYFP signal (magenta) were segmented using the blob finder algorithm of Arivis Vision4D for foci identification, as described in the Methods section. White arrows indicate the co-localized condensates. The enlarged images of co-localized foci are shown insets at the bottom. Scale bars: 2 μm. (**B**) Quantification of size of FCA (total FCA-mTurquoise identified foci), FLL2 (total FLL2-eYFP identified foci) and FCA identified foci that are co-localized with FLL2. The lines in the violin plots indicate the median and quartiles. (**C**) Size and frequency distribution of FCA, FLL2 foci and FCA foci that are co-localized with FLL2. (**D**) Number of FCA, FLL2 foci and FCA foci that are co-localized with FLL2 in each nucleus. The lines in the violin plots indicate the median and quartiles. The quantitative analysis was based on 18 nuclei from 5 independent samples. Statistical significance was determined using non-parametric Brunner-Munzel test. ****P-value < 0.001.

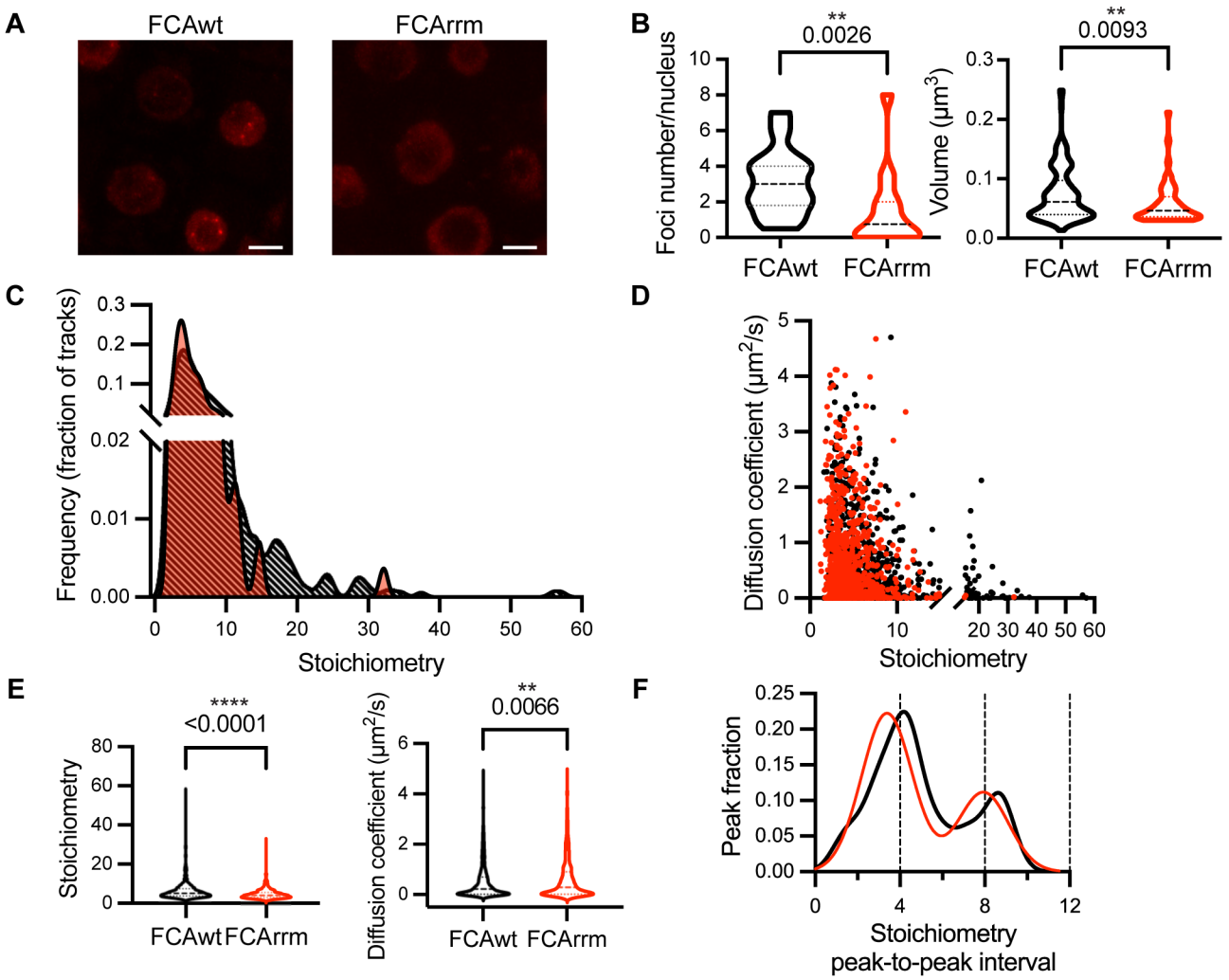

Figure 3. The RNA-binding activity of FCA influences FCA condensate size and number
(A) Selected Airyscan confocal images of wild type FCA fused to mScarlet-I (FCAwt) and FCA-mScarlet-I with the missense (L304F) mutation (FCArrm). Scale bars: 5 µm. (B) Quantification of size and number of FCAwt and FCArrm condensates using Vision4D software. The lines in the violin plots indicate the median and quartiles. The quantitative analysis is based on 43 FCAwt nuclei and 65 FCArrm nuclei from 3 independent experiments. (C) Distributions of stoichiometry of individual FCAwt (black) and FCArrm (red) particles. (D) Diffusion coefficient and stoichiometry of each FCAwt (black) and FCArrm (red) particle. (E) Statistic analysis of stoichiometry and diffusion coefficient of FCAwt and FCArrm particles. (F) Periodicity of FCAwt (black) and FCArrm (red) particle stoichiometry. The single particle tracking analysis is from 3 biologically independent experiments. The FCAwt data corresponds to that shown in Figure 1. Statistical significance was determined using non-parametric Brunner-Munzel test. ***P*-value < 0.01, *****P*-value < 0.0001. Results from individual replicates are provided in Appendix Figure S3 and S5.

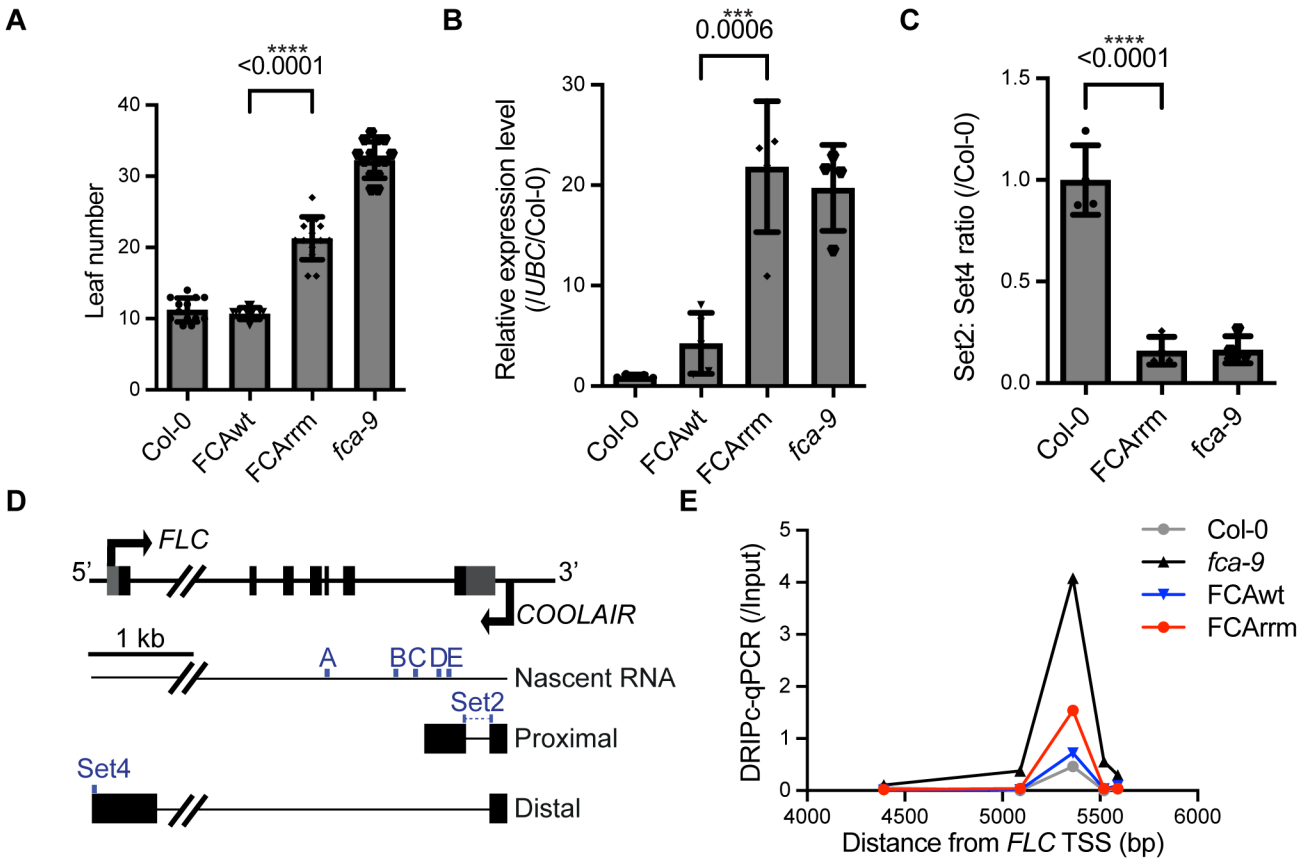

Figure 4. A missense mutation in the RRM of FCA only partially complements the *fca-9* mutant phenotype

(**A**) Flowering time of selected transgenic lines (#8 for FCAwt and #1 for FCArrm in Fig. EV1) grown in a long-day photoperiod. Data are presented as mean ± s.d. (n = 14, except for Col-0 which n = 13). (**B**) Relative values of *FLC* in the indicated lines. Values were normalized to the *UBC* gene and to Col-0. Data are presented as mean ± s.d. (n = 5, except for *fca-9* where n = 4). (**C**) The ratio of proximal: distal isoforms of *COOLAIR* transcripts relative to control (Col-0) in the indicated plants. Data are presented as mean ± s.d. (n = 4). (**D**) Schematic of *FLC* and *COOLAIR* transcripts at the *FLC* locus. Blue dots indicate the locations of primer sets for qPCR. Untranslated regions are indicated by grey boxes, and exons by black boxes. kb, kilobase. (**E**) DRIPc–qPCR analyzing *COOLAIR* R-loop in indicated genotypes. Data are presented as mean from four technical repeats. Three biological replicates show similar trends (Appendix Figure S7). TSS, transcription start site. The primer sets used for DRIPc-qPCR (A to E) corresponds to that shown in Fig. 4D. Statistical significance was calculated using the two-tailed t-test, with *P*-values indicated. ****P*-value < 0.001, *****P*-value < 0.0001.

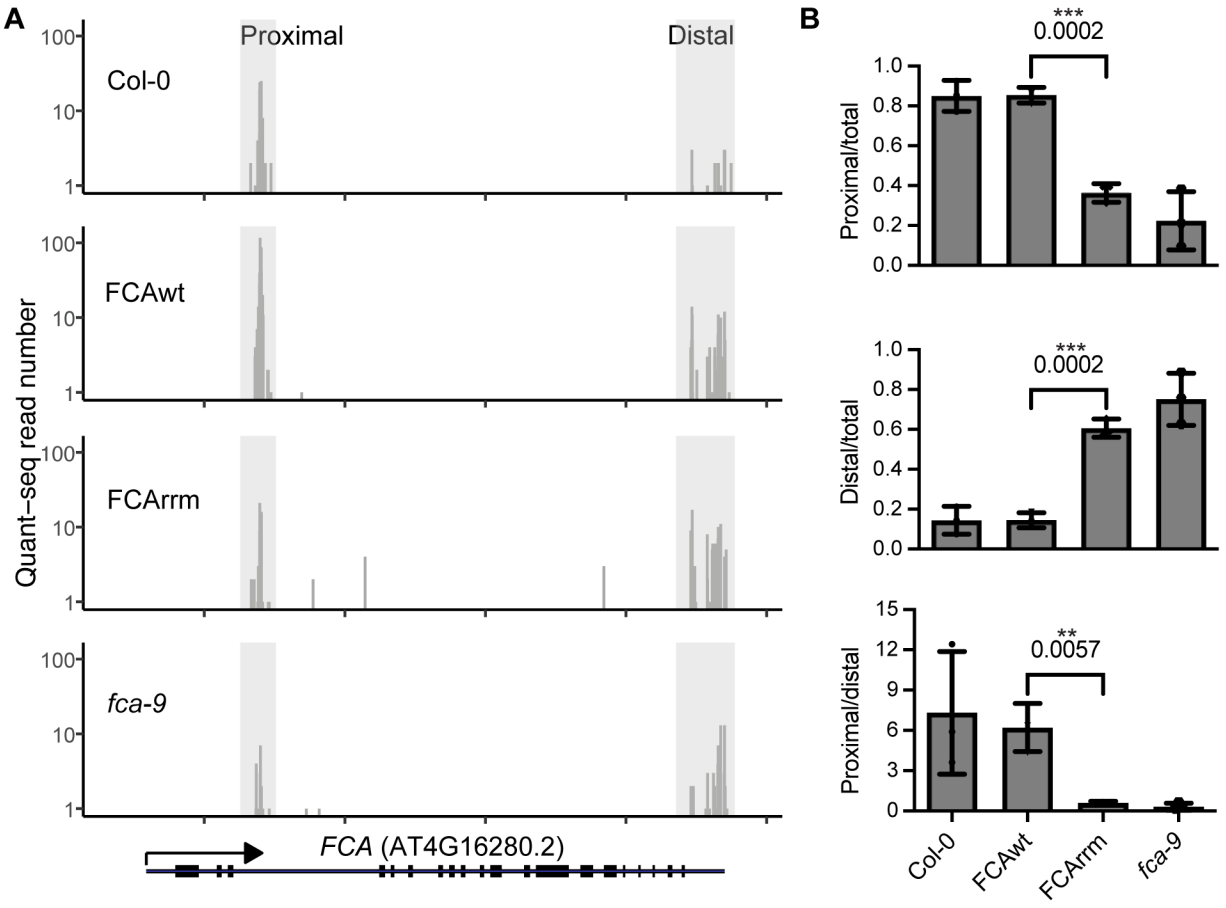

Figure 5. The rrm mutation perturbs the autoregulatory function of FCA in promoting proximal polyadenylation

(**A**) Quant-seq experiments assaying polyA sites at the *FCA* locus in different genotypes. The vertical pale grey bars highlight previously described proximal and distal polyA sites. (**B**) Quantification of reads corresponding to proximal and distal polyadenylated *FCA* transcripts. Data are presented as mean ± s.d. (n = 3). Statistical significance was calculated using the two-tailed t-test, with *P*-values indicated. ***P*-value < 0.01, ****P*-value < 0.001.

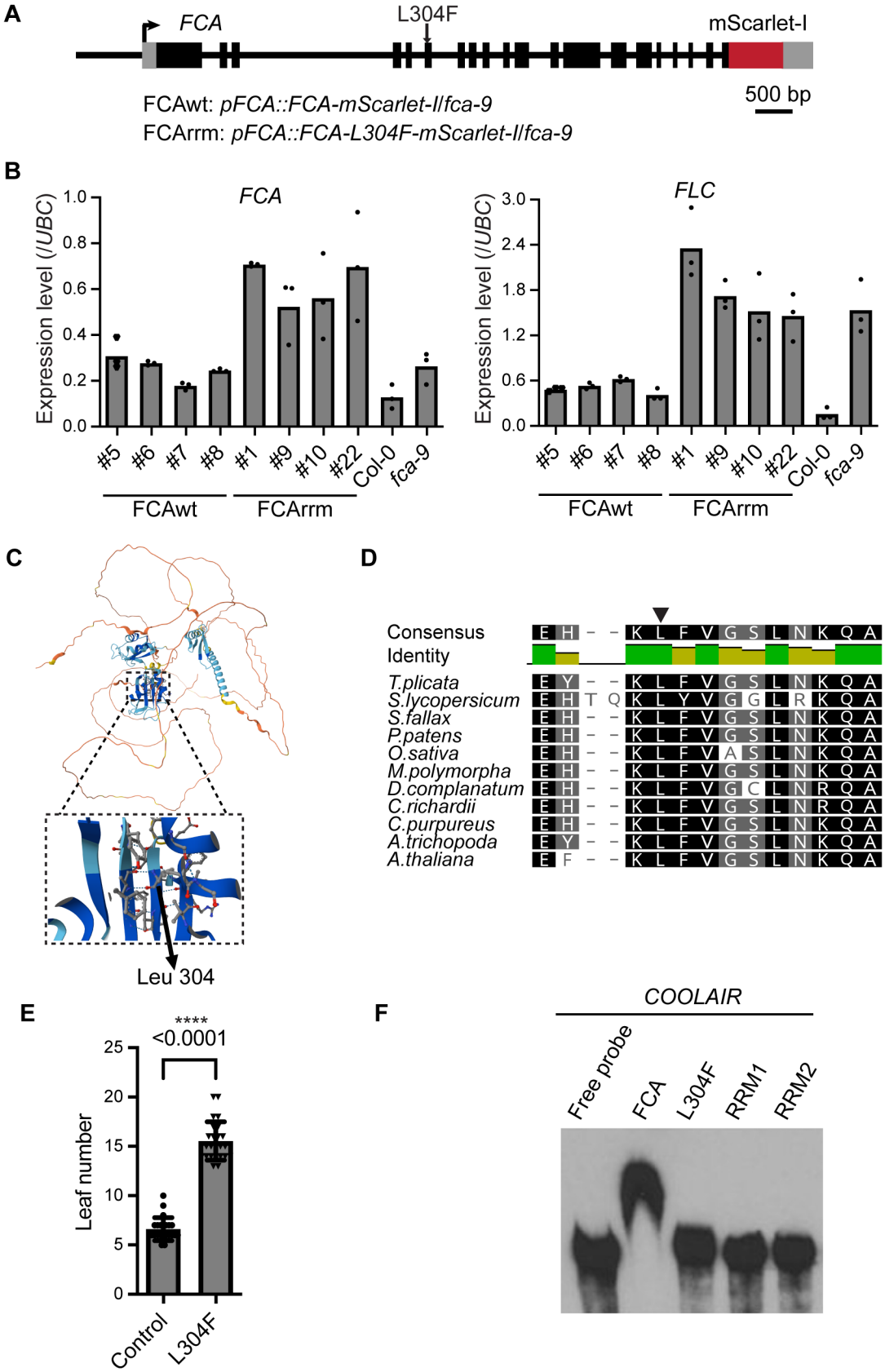

Figure EV1. A missense mutation (L304F) on the second RRM of FCA attenuates RNA-binding
(**A**) Schematic representation of the transgenic FCA-mScarlet-I fusion within the FCA locus - the position of the missense L304F mutation is indicated. Untranslated regions are indicated by grey boxes, exon regions by black boxes, and mScarlet-I coding sequence by the red box. (**B**) Expression of *FLC* and *FCA* relative to *UBC* in plants at the T3 generation following transformation. Data represent mean values from technical repeats. The FCAwt #8 and FCArrm #1 lines are used for further analysis. (**C**) FCA protein structure predicted by Alphafold Protein Structure Database (AF-Q5I5A2-F1-v4, Jumper et al, 2021; Varadi et al, 2022). The arrow indicates the location of the amino acid change from the missense mutation (amino acid 213 in this protein structure database corresponds to amino acid 314 when FCA uses the non-canonical start CTG codon). (**D**) Peptide alignment of Arabidopsis FCA proteins from different plant species (https://phytozome-next.jgi.doe.gov). The arrow indicates the conserved Leucine 304. (**E**) Plants carrying transgenes with the L304F mutation show delayed flowering compared to the control. Data are mean ± s.d. (n = 23 and 24 for the control and L304F, respectively). Statistical significance was calculated using the two-tailed t-test, with *P*-value indicated. ****P-value < 0.0001. (**F**) *In vitro* RNA binding assay showing that the Leu 304 and each RRM domain are important.

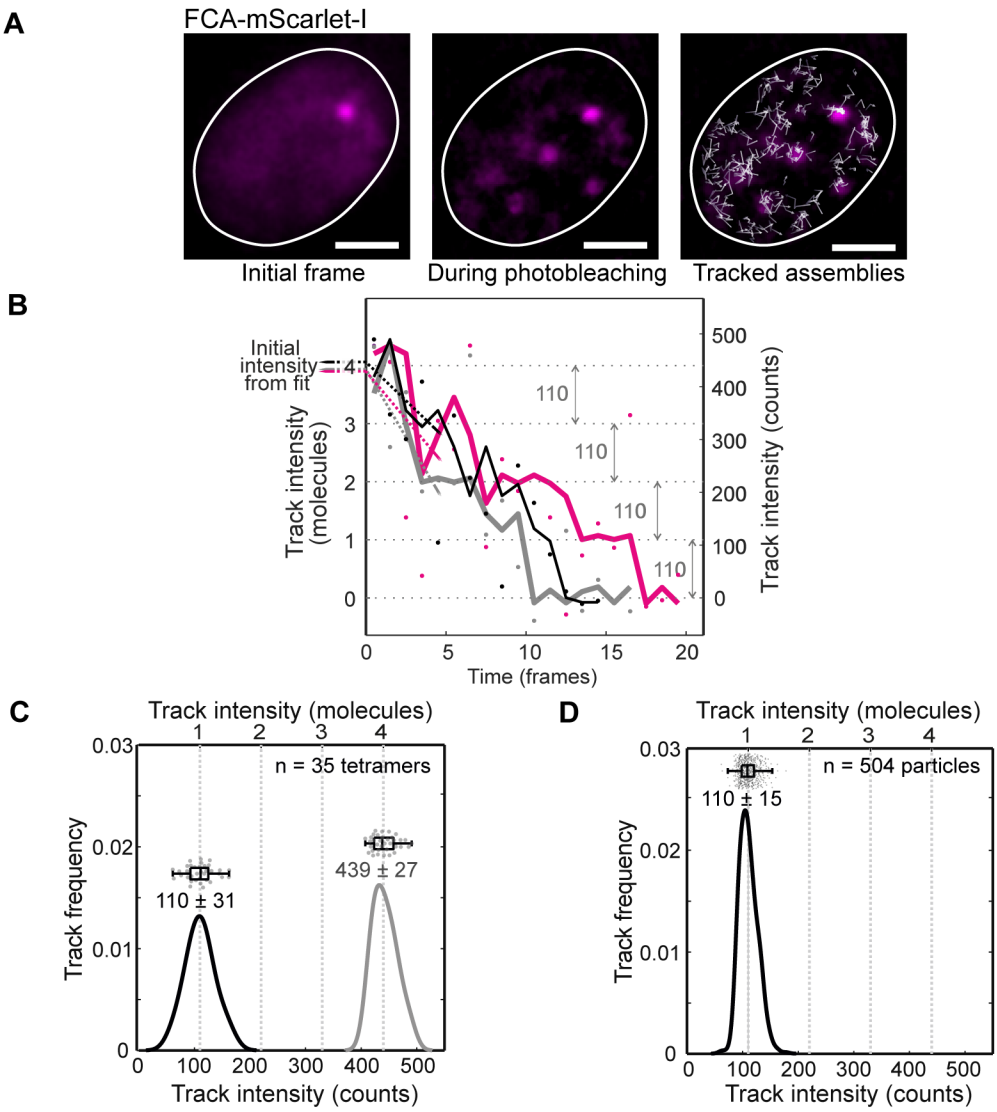

Figure EV2. Automated tracking analysis of FCA particles and determination of the characteristic single molecule brightness in living tissues.
(**A**) An example of FCA-mScarlet-I particle tracking at 10 ms/frame, which intermediate frame overlaid with tracks (white arrows) corresponding to the paths of achieves super-resolved localization precision and provides estimates of the corresponding stoichiometry and mobility. The left panel shows the initial frame of the acquisition, while the middle panels display the intermediate stage of the acquisition (after 75 ms), where contrast is greatest and assemblies are clearly visible. The nuclear boundary (white closed line) is obtained by blurring the initial frame and setting the Otsu intensity threshold. The third panel features the same ach detected assembly throughout the acquisition. Scale bar: 2 µm. (**B**) The consistent photobleaching steps yield an estimate of about 110 photoelectron counts for the characteristic single-molecule brightness of the FCA-mScarlet-I *in planta*. The intensity of particles near the end of five particle tracks in the FCA-mScarlet-I image sequences is represented by square dots, and the denoised signals by solid lines of the corresponding color. Here, zero intensity corresponds to the mean background level after complete photobleaching. (**C**) A subset of n = 35 particles was identified as having four photobleaching steps. This subset gives a characteristic single molecule brightness (black line) of 110 ± 31 counts (mean ± s.d., n=35). The initial intensities of these particles (grey line) are each greater than the characteristic single molecule brightness by a factor of ~ four (stoichiometry: 4.0 ± 0.6 molecules, mean ± s.d., n=35), suggesting that each particle is composed of ~ 4 FCA-mScarlet-I molecules. Data for individual particles are shown above the corresponding distribution in a jitter and box plot (showing median, interquartile range and min-max range). (**D**) A characteristic single molecule brightness of 110 ± 15 counts (mean ± s.d., n=504) is calculated from the time-averaged intensity levels of each of n=504 particles photobleached to a single molecule above background, sifted using the signal-to-noise threshold.

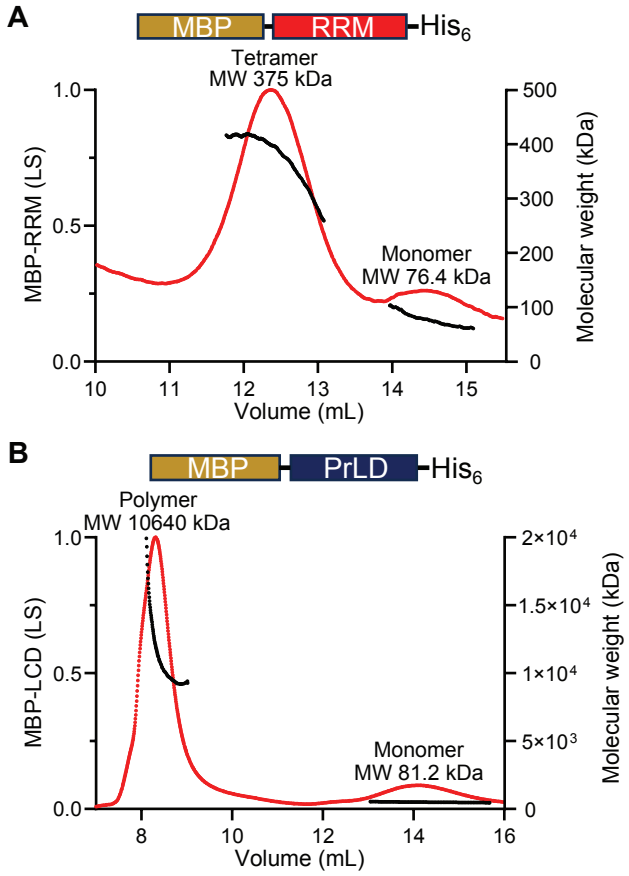

Figure EV3. SEC-MALS of purified FCA truncated proteins

SEC-MALS of purified MBP-RRM (**A**) or MBP-PrLD (**B**). Line traces indicate molar mass as determined from MALS. The predicted molecular mass of MBP fused FCA truncated protein MBP-RRM and MBP-PrLD is approximately 72 kDa and 89 kDa, respectively.

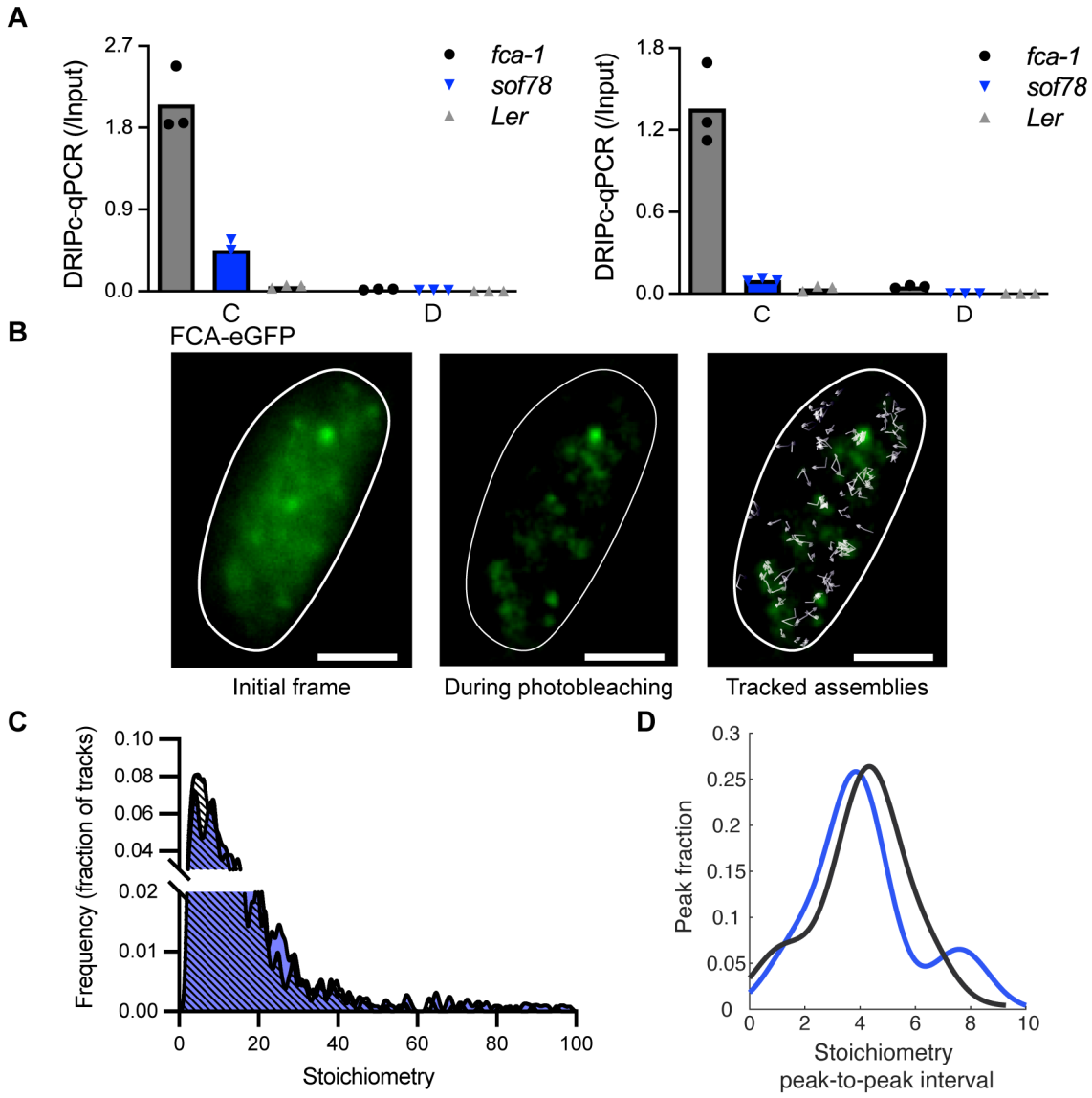

Figure EV4. The *COOLAIR* R-loop level and FCA-eGFP single particle tracking in the *sof78* mutant
(**A**) Two biological replicates of DRIPc–qPCR *COOLAIR* R-loop in the L*er*, *sof78* and *fca-1* genotypes. The *sof78* mutant carries a missense mutation in a region of FLL2 that is predicted to form a salt bridge, which influences FCA condensation (Fang *et al*., 2019). Data are means from three technical repeats. TSS, transcription start site. The primer sets used for DRIPc-qPCR (C and D) are the same as those shown in Figure 4D. (**B**) An example of FCA-eGFP particle tracking at 10 ms/frame. The left panel shows the initial frame of the acquisition. The third panel features the same intermediate frame overlaid with tracks (white arrows) corresponding to the paths of each detected assembly throughout the acquisition. The nuclear boundary (white closed line) is obtained by blurring the initial frame and setting the Otsu intensity threshold. Scale bar: 2 µm. (**C**) Distributions of stoichiometry of individual FCA-eGFP (black) and FCA-eGFP/*sof78* (blue) particles. (**D**) Periodicity of FCA-eGFP (black) and FCA-eGFP/*sof78* (blue) particle stoichiometry. The stoichiometry in the figure is capped at 100. The single particle tracking analysis is from three biologically independent experiments.

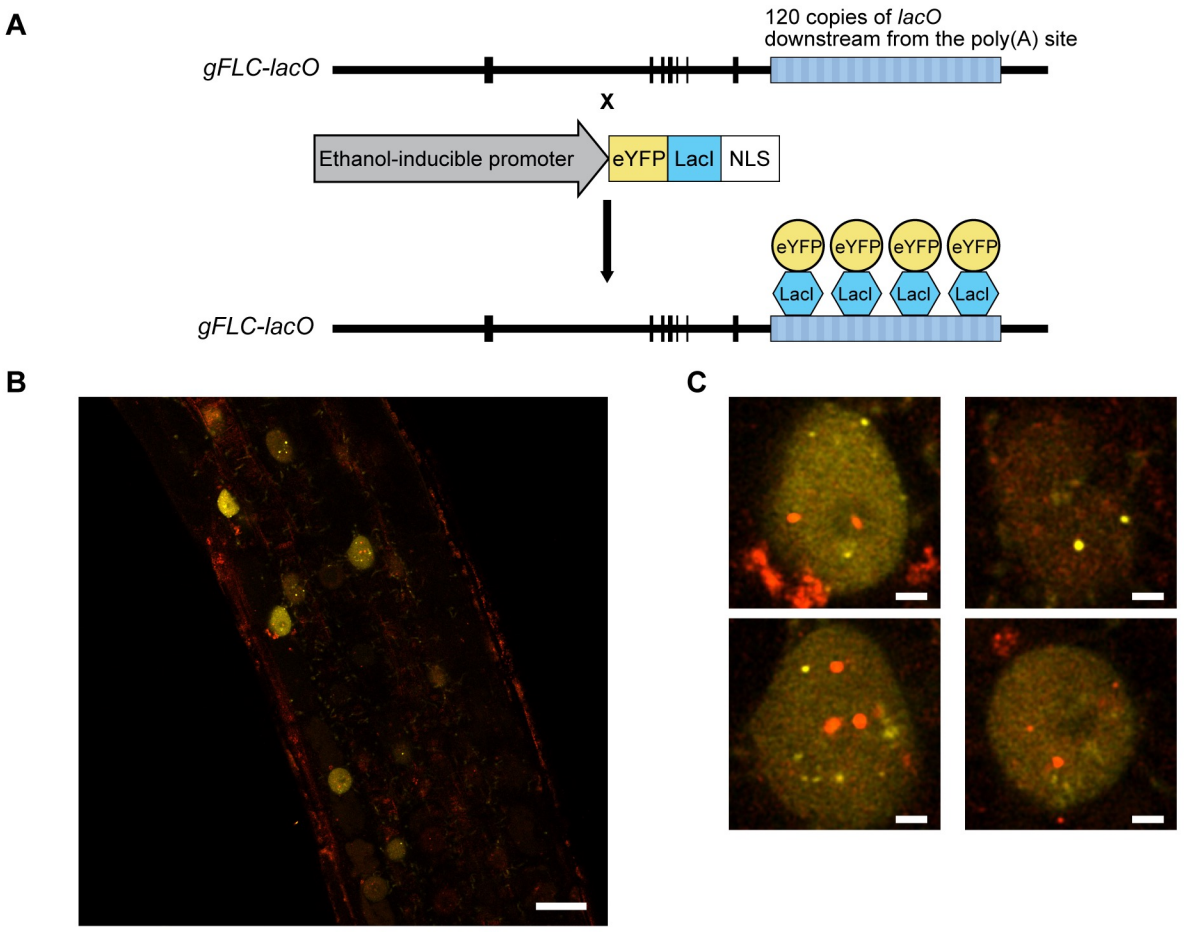

Figure EV5. Co-localization analysis of FCA condensates and *FLC-lacO*/eYFP-LacI
(A) An illustration of the *FLC-lacO*/eYFP-LacI transgenic plants. (B) Single slice of Arabidopsis root Airyscan image showing expression of FCA-mScarlet-I (red) and *FLC-lacO*/eYFP-LacI (yellow) in nuclei. Scale bars: 20 µm. (C) Subsets of Airyscan images from B showing nuclei co-expressing FCA condensates (red) and *FLC-lacO*/eYFP-LacI (yellow). Scale bars: 2 µm. The FCA-mScarlet-I and LacI-eYFP signals were enhanced by shifting their dynamic ranges to 0–1099 and 0–4220 in EV5B, and to 0–1000 and 0–6000 in EV5C. The images were acquired on a Zeiss LSM980 using LD C-Apochromat 40x/NA 1.1 water-immersion objective. The fluorescent proteins, eYFP and mScarlet-I, were excited at 488 and 561 nm, respectively.

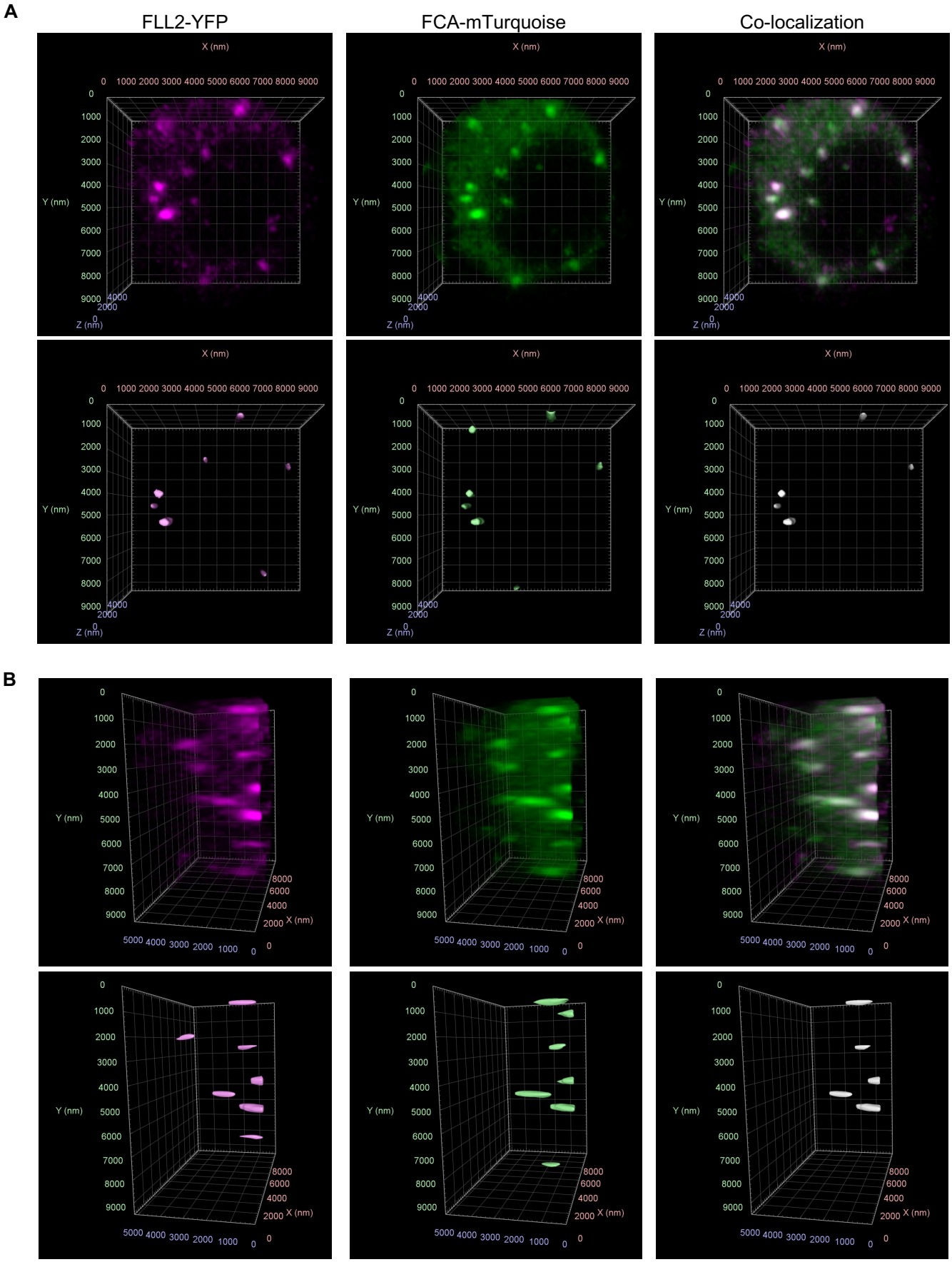

Appendix Figure S1.

The co-localization of 3D images is achieved after object identification using the blob finder algorithm

Front view (A) and side view (B) of the 3D image with grid lines, consistent with Figure 2A, illustrating the FCA-mTurquoise, FLL2-eYFP, and the objects identified using the blob finder algorithm, as described in the Methods. In the identified objects, green dots denote FCA-mTurquoise identified foci, magenta dots indicate FLL2-eYFP foci identified, and the white region highlights the co-localised area.

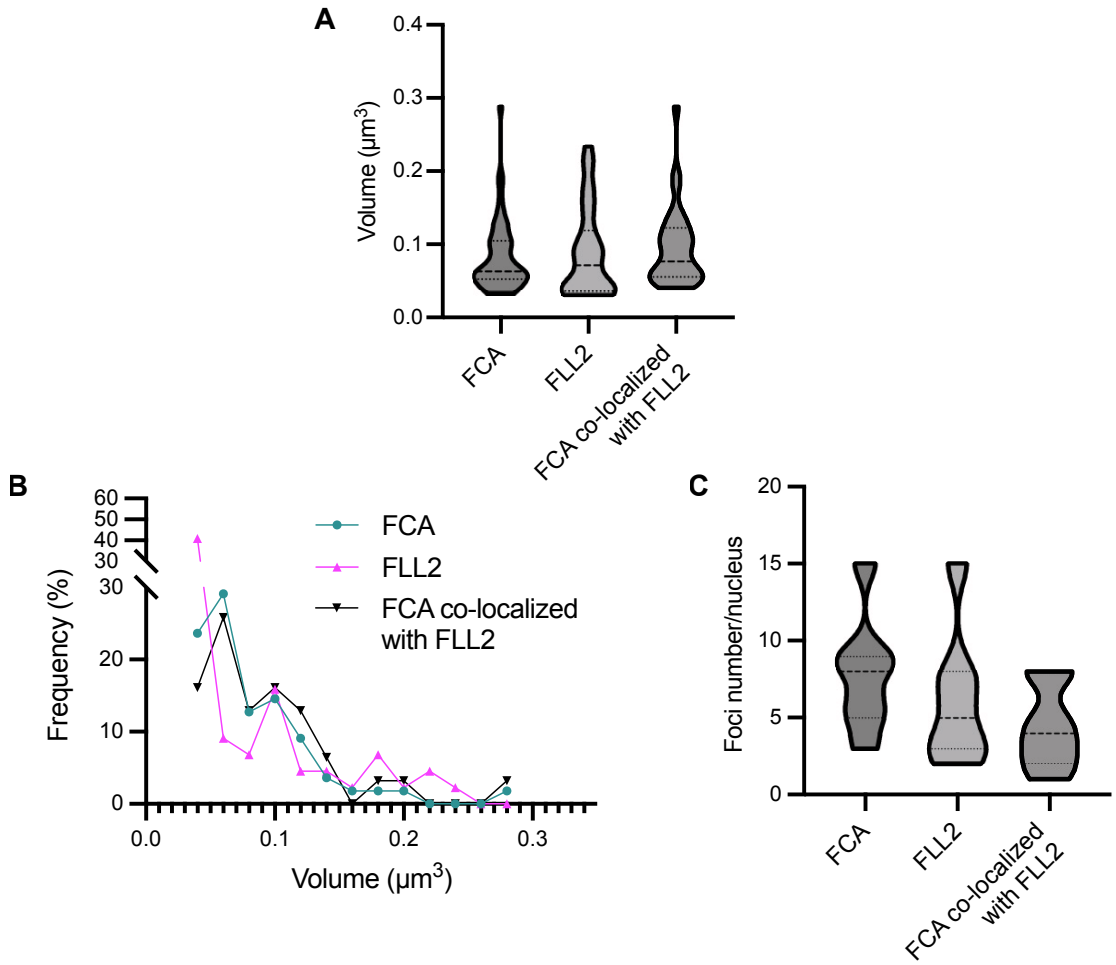

Appendix Figure S2. An additional experiment analysing the co-localization of FCA and FLL2
(A) Quantification of size of FCA (total FCA-mTurquoise identified foci), FLL2 (total FLL2-eYFP identified foci) and FCA identified foci that are co-localized with FLL2. The lines in the violin plots indicate the median and quartiles. (B) Size and frequency distribution of FCA, FLL2 foci and FCA identified foci that are co-localized with FLL2. (C) Number of FCA, FLL2 foci and FCA foci that are co-localized with FLL2 in each nuclei. The lines in the violin plots indicate the median and quartiles. The images for the quantification were acquired on a Zeiss LSM980 using LD C-Apochromat C-Apochromat 63x/NA 1.2 water-immersion objective. The fluorescent probes, mTurquoise2 and eYFP, were excited at 458 and 514 nm, respectively. The voxel size of images for quantification analysis was 0.05 μm x 0.05 μm x 0.21 μm (xyz). The quantitative analysis was based on 7 nuclei.

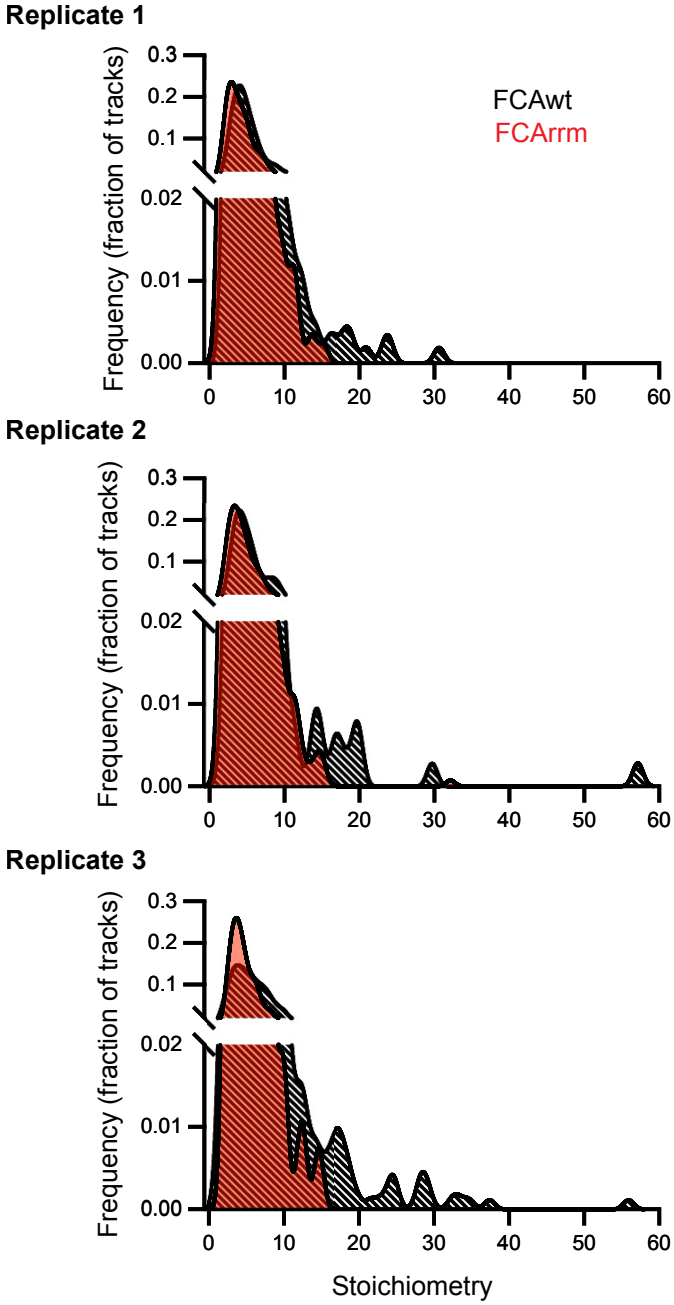

Appendix Figure S3. Stoichiometry distribution of individual FCA particles in FCAwt and FCArrm genotypes in different experiments

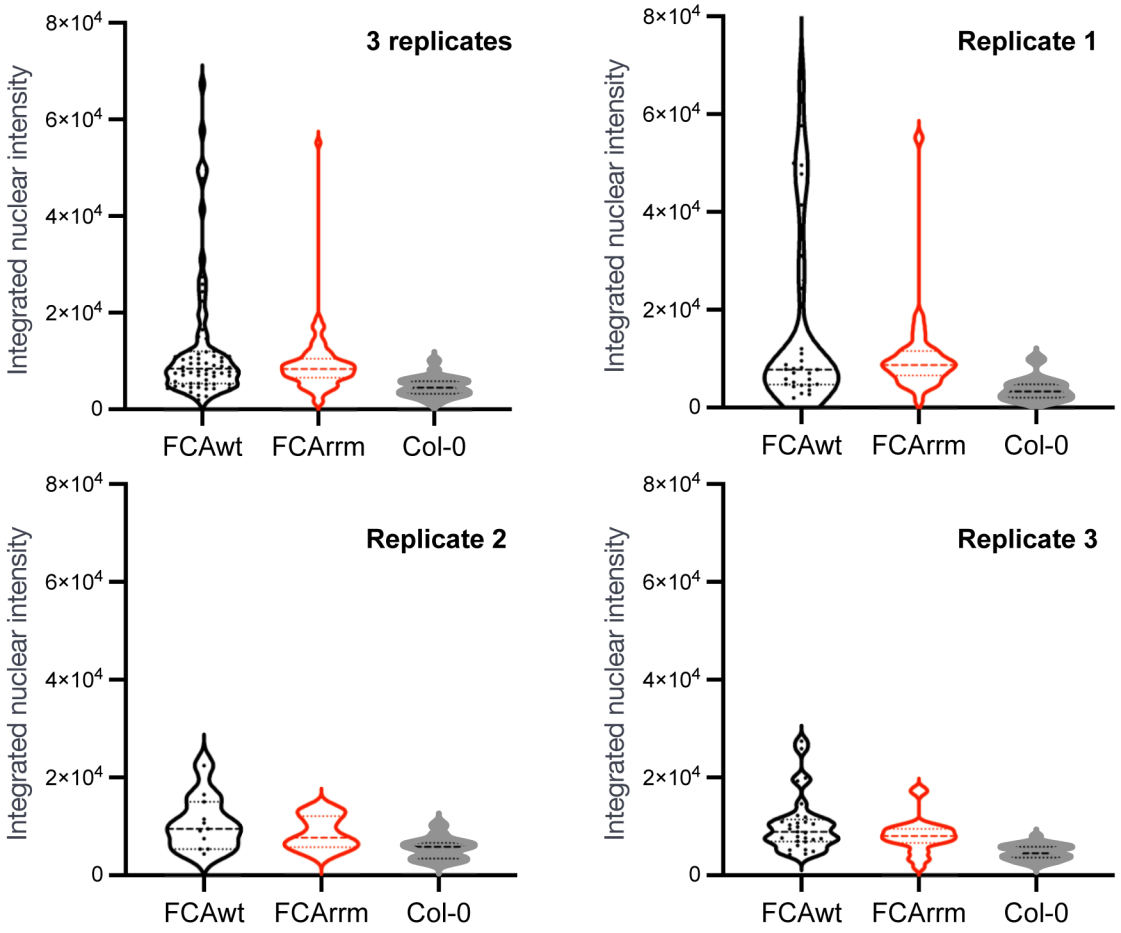

Appendix Figure S4. Integrated nuclear intensity in FCAwt and FCArrm genotypes from different experiments

The violin plots represent the integrated nuclear intensity (in molecules) of FCA reporters in FCAwt and FCArrm from each biological replicate. Col-0 is negative control.

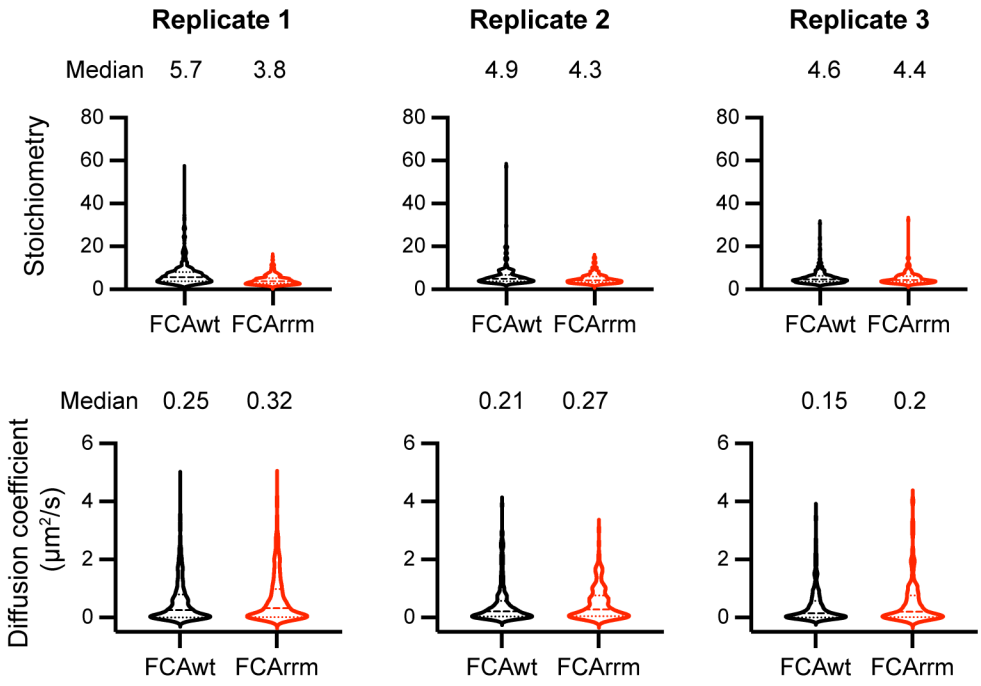

Tracking number				
	Replicate 1	Replicate 2	Replicate 3	Total
FCAwt	504	202	302	1008
FCArrm	560	171	182	913

Appendix Figure S5. Quantification of FCA particle stoichiometry and diffusion coefficient
The violin plots represent the FCA reporter stoichiometry and diffusion coefficient in FCAwt and FCArrm from each biological replicate. The table displays the sample statistics used for quantitative SlimVar analysis, including the numbers of tracks.

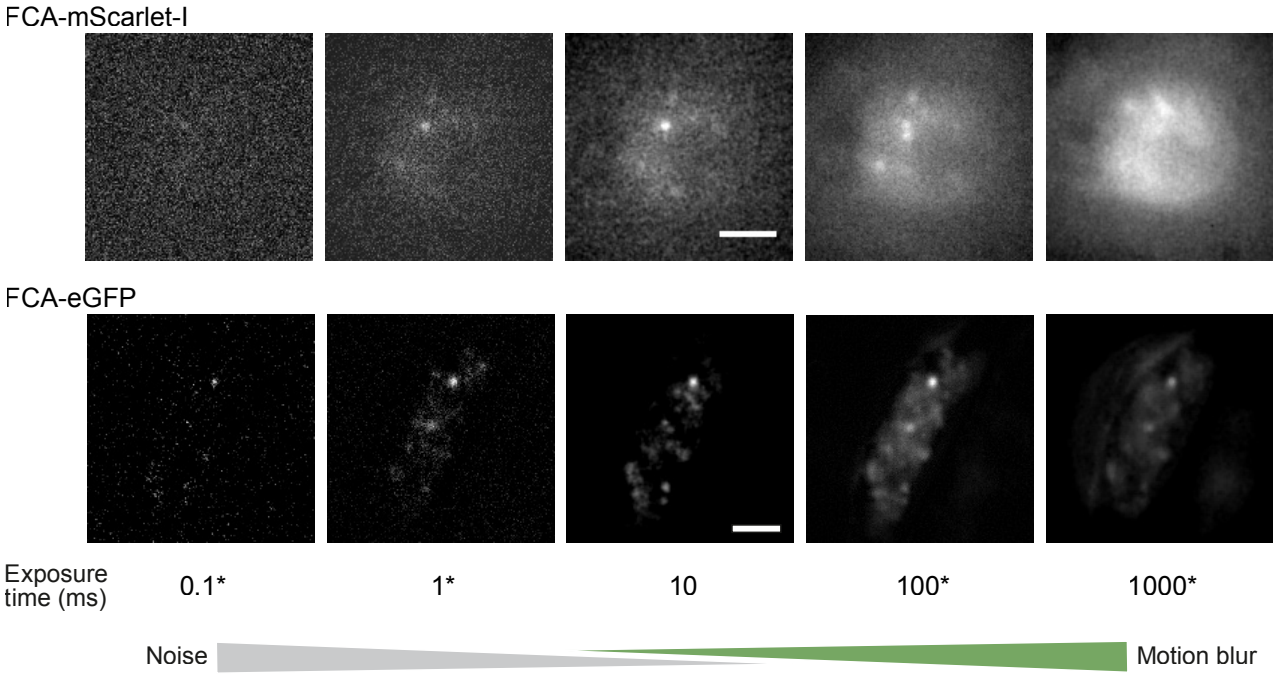

Appendix Figure S6. SlimVar at 10 ms/frame provides optimal contrast for detection of FCA-mScarlet-I and FCA-eGFP particles

A single acquisition at 10 ms/frame exposure was used to simulate a range of exposure times (labelled with *). Longer exposure times were generated by summing 10 or 100 frames directly, while shorter exposures were created by dividing a frame's pixel intensity by 10. This was done either with FCA-mScarlet-I or FCA-eGFP. Frames are displayed with individual min/max contrast stretching. Below 1 ms/frame, shot noise reduces the contrast to a level insufficient for observing single molecules, whereas at 100 ms/frame, motion blur and photobleaching degrade the contrast for all but the brightest and least mobile assemblies. Scale bar: 2 µm.

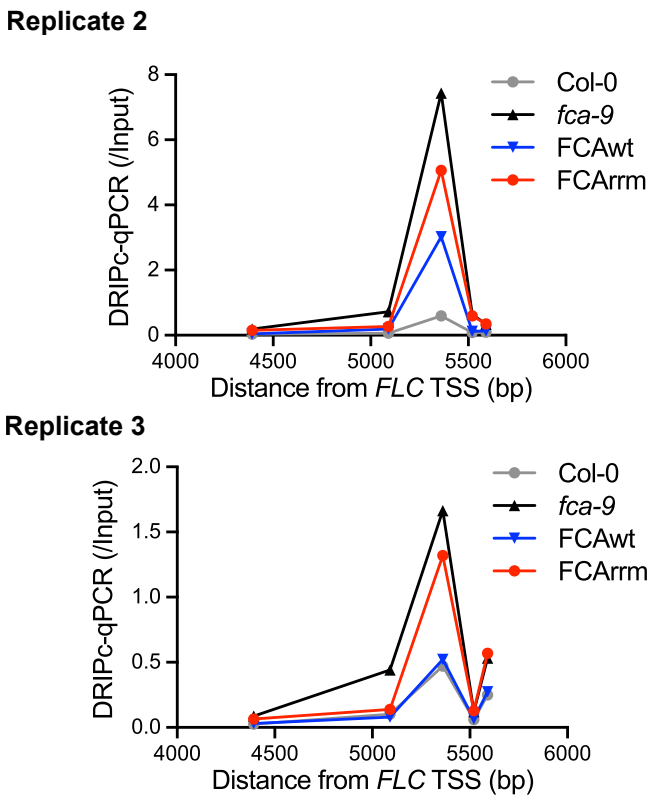

Appendix Figure S7. Two additional independent DRIPc–qPCR experiments were performed to analyze the *COOLAIR* R-loop in the indicated genotypes

Data are presented as mean from four technical repeats for Replicate 2 and three technical repeats for Replicate 3. TSS, transcription start site. The primer sets used for DRIPc-qPCR (A to E) corresponds to that shown in Figure 4D.